Journal of Environmental Chemical Engineering 13 (2025) 116857

Contents lists available at ScienceDirect

Journal of Environmental Chemical Engineering

journal homepage: www.elsevier.com/locate/jece

Enhanced piezo-induced photocatalytic activity of $BaTiO_3/Cd_{0.5}Zn_{0.5}S$ S—scheme heterojunction for water pollution remediation: Performance, degradation pathway, and toxicity evaluation

Tshepo T. Mohlala [a], Tunde L. Yusuf [b], Mike Masukume [c], Vincent Ojijo [c], Nonhlangabezo Mabuba [a,d,*]

[a] University of Johannesburg, Department of Chemical Science, Doornfontein Campus, Johannesburg 2028, South Africa
[b] Department of Chemistry, Faculty of Natural and Agricultural Sciences, University of Pretoria, Private Bag X20, Hatfield, Pretoria 0028, South Africa
[c] Council for Scientific and Industrial Research (CSIR), Pretoria Campus, Pretoria 0001, South Africa
[d] Centre for Nanomaterial Science Research, Department of Chemical Sciences, Doornfontein Campus, Johannesburg 2028, South Africa

ARTICLE INFO

Keywords:
Piezocatalysis
Pharmaceutical
Degradation pathway
S—Scheme
$BaTiO_3$
Wastewater
Toxicity

ABSTRACT

Pharmaceutical pollutants in water pose a threat to ecosystems and human health by disrupting aquatic life, contributing to antibiotic resistance, and causing hormonal imbalances and increased disease susceptibility in humans. Thus, we report the fabrication of a novel $BaTiO_3/Cd_{0.5}Zn_{0.5}S$ heterojunction for the piezo-photocatalytic degradation of ciprofloxacin (CIP) in wastewater. The $BaTiO_3/Cd_{0.5}Zn_{0.5}S$ was synthesized via solvothermal deposition of $Cd_{0.5}Zn_{0.5}S$ (CZS) onto $BaTiO_3$ (BTO) nanorods. This heterojunction exhibited superior photocatalytic activity, degrading ciprofloxacin ~85 % and ~3 times more effectively than pristine CZS and BTO, respectively. Its enhanced piezo-photocatalytic performance is attributed to the induced piezoelectric effect, sulfur defects, internal electric field, and S-Scheme charge transfer. Scavenger studies identified h^+, O_2^-, and $^{\bullet}OH$ as the major reactive species responsible for CIP degradation. After 90 min, the extent of mineralization reached 46.7 %, and intermediate products were evaluated using Ultra-performance liquid chromatography-mass spectrometry(UPLC-MS), with their toxicity assessed using the Toxicity Estimation Software Tool (T.E.S.T). The catalyst demonstrated excellent stability over four reuse cycles. The successful development of the BTO/CZS heterojunction holds significant promise for advancing environmentally sustainable water treatment and pollution remediation technologies.

1. Introduction

Water pollution, primarily caused by organic pollutants, poses a substantial environmental and health risk [1,2]. Among these pollutants, pharmaceuticals, particularly antibiotics, are persistent. Antibiotics, commonly utilized in both agricultural and healthcare sectors, are known for their stability, resulting in approximately 75 % of ingested antibiotics being excreted into water streams [3]. The growing issue of antimicrobial resistance in the environment is due to the increasing presence of these emerging contaminants, mainly antibiotics [4]. The development of advanced oxidation processes (AOPs) for the breakdown of these contaminants has become a necessity as conventional treatment systems struggle to remediate and effectively remove the pollutants [5–7].

Piezo-photocatalysis is an emerging AOPs that harnesses the combined power of piezoelectricity and photocatalysis to achieve superior catalytic performance [8–10]. Piezoelectric materials, lacking a symmetrical center, generate an internal electric field when subjected to pressure. This pressure alters the material's bandgap structure, creating a voltage and a separation of charges within the crystal lattice [11]. In photocatalysis, light excites electrons in a semiconductor, generating electron-hole pairs [12]. These act as powerful oxidizing and reducing agents for pollutant degradation, but their effectiveness is hampered by rapid recombination. Here's where the magic happens. The electric field from piezoelectricity acts as a driving force in piezo-photocatalysis, separating the electron-hole pairs and significantly reducing recombination [13,14]. This ensures a greater abundance of reactive species available for pollutant degradation, leading to a marked improvement in

* Corresponding author at: University of Johannesburg, Department of Chemical Science, Doornfontein Campus, Johannesburg 2028, South Africa.
E-mail address: nmabuba@uj.ac.za (N. Mabuba).

https://doi.org/10.1016/j.jece.2025.116857
Received 22 January 2025; Received in revised form 25 April 2025; Accepted 28 April 2025
Available online 4 May 2025
2213-3437/© 2025 The Author(s). Published by Elsevier Ltd. This is an open access article under the CC BY-NC-ND license (http://creativecommons.org/licenses/by-nc-nd/4.0/).

overall catalytic performance. This technology holds great promise for a variety of applications and is not limited to wastewater treatment [15].

While piezo-photocatalysis accelerates the generation of reactive species, it does not inherently solve the issue of photogenerated carrier recombination in semiconductor technology [16,17]. This recombination occurs when generated electrons (e^-) and holes (h^+) due to light absorption in a photocatalyst recombine, limiting the efficiency of the photocatalytic process. To address this drawback, the S-scheme charge transfer mechanism has emerged as a promising solution. In an S-scheme heterojunction, two semiconductors are selected with staggered band gaps: one acting as an oxidation photocatalyst and the other as a reduction photocatalyst [18]. The oxidation photocatalyst has a more positive valence band potential, while the reduction photocatalyst has a more negative conduction band potential [19]. When light excites these semiconductors, electrons from the oxidation photocatalyst's conduction band recombine with holes in the reduction photocatalyst's valence band at the interface [20]. This recombination effectively reduces the likelihood of bulk recombination within each semiconductor. As a result, this leaves the remaining high-energy holes and electrons in the valence band and conduction band of the oxidation photocatalyst and conduction oxidation photocatalyst available for redox reactions, respectively [21]. The high-energy holes can oxidize water or hydroxide ions to generate hydroxyl radicals ($^{\bullet}OH$), which are highly reactive species crucial for degrading organic pollutants [22]. Meanwhile, the high-energy electrons can reduce oxygen molecules to form superoxide radicals ($O_2^{\bullet-}$), further contributing to the degradation process [23,24]. Thus, the S—S-scheme charge transfer mechanism enhances photocatalytic efficiency by reducing the recombination rate of photogenerated carriers, facilitating efficient charge separation, and increasing the production of reactive oxidants like superoxide and hydroxyl radicals [19,25]. Thus, the choice of semiconductors is very crucial to the efficiency of the piezo-photocatalysis.

Due to its impressive piezoelectric coefficient and dielectric constant, $BaTiO_3$ is considered one of the best piezoelectric nanomaterials [26]. BTO has been used as a lead-free piezo-active material in piezoelectric applications such as health (tissue engineering) [27], osseointegration, and many more. The synergy between BTO and other photocatalytic semiconductors has been explored to greatly improve charge carrier separation through mechanical force at the heterostructure interface [28]. This process depends on spontaneous polarization in the ferroelectric material, which is responsible for generating the piezo-potential (internal electric field), enhancing the charge separation in piezo-photocatalysis [29]. Some of the reported $BaTiO_3$ composites in piezo-photocatalysis are $BaTiO_3/TiO_2$ [30], $BaTiO_3/Ag_3PO_4$ [31], $BaTiO_3/CuPbSbS_3$ [32], and $BaTiO_3$@C [33]. The need for modification of BTO arises due to its current drawbacks, such as a wide band gap (2.8–3.2 eV) limiting its light absorption properties.

$Cd_xZn_{1-x}S$ is a ternary nanomaterial made up of CdS and ZnS. CZS is an n-type semiconductor with an energy bandgap (2.5 eV) commonly used in solar cells due to its potential cost-reduction [34,35]. ZnS is also an n-type semiconductor belonging to the II-IV group of semiconductors with a wide energy band gap (3.7–3.8 eV) [36]. ZnS aids in reducing light absorption losses at the interface of CdS [28]; for that reason, these semiconductors have been used in various applications, such as optics, optoelectronics, and electronic industries [37]. CZS is a promising photocatalytic material as it brings interesting new properties with tunable energy bandgaps depending on the structure and possesses the potential to be used in optoelectronic devices such as photoconductors and photoluminescent materials [38–40]. Their optical properties can be good for photovoltaic applications, photocatalysis, and piezoelectric-assisted photocatalytic processes [41–43]. Because of its high conduction band, it can serve as an excellent reduction photocatalyst.

Considering the high conduction band of CZS and the low valence band of BTO, along with their previously reported photo-piezoelectric properties, we synthesized a novel $BaTiO_3/Cd_{0.5}Zn_{0.5}S$ heterostructure using a solvothermal synthesis process, anticipating the formation of an S-scheme heterojunction. The catalyst utilized the synergistic effects of ultrasonication and light illumination to generate oxidants for the efficient oxidation of ciprofloxacin. The enhanced charge separation suppressed recombination rate and extended carrier lifetime contribute significantly to the photocatalytic degradation efficiency of $BaTiO_3$ through the formation of a hybrid heterostructure with the piezo-active photocatalyst CZS. This represents a significant advancement in piezo-photocatalysis for oxidation processes.

2. Experimental section

2.1. Reagents

Cadmium acetate dihydrate ($Cd(CH_3COO)_2{\bullet}2H_2O$, 98.0 %) was purchased from BDH Labs. Ethylenediaminetetraacetic acid (EDTA, 98.0 %) was purchased from Fluka Chemicals. Sodium hydroxide (NaOH, purified, 97 %), potassium hydroxide (KOH, extrapure, 85 %), and titanium isopropoxide ($C_{16}H_{36}O_4Ti$, TTIP, extra pure, 28.6 %) were purchased from Sisco Research Laboratories. Sodium sulfate (Na_2SO_4, Analytical reagent) was acquired from Sachelle Chemicals. Barium hydroxide octahydrate ($Ba(OH)_2{\bullet}8H_2O$, extrapure AR, 98.0 %), zinc acetate dihydrate ($Zn(CH_3COO)_2{\bullet}2H_2O$, polyvinylidene fluoride (PVDF, 99.0 %), N-methyl-2-pyrrolidone (NMP, 99.0 %), potassium chloride (KCl, 99 %), polyvinylpyrrolidone (PVP, 99 %), potassium hexacyanoferrate tetrahydrate (II) ($K_4Fe(CN)_6{\bullet}3H_2O$, 98.5 %), acrylamide solution (C_3H_5NO, AR), potassium hexacyanoferrate (III) ($K_3Fe(CN)_6$, ACS reagent), ethylene glycol (EG, 99.8 %), tert-Butanol (t-BuOH, 99.7 %, ACS Reagent), thioacetamide (C_2H_5NS, 99 %), formic acid (HCOOH, 98 %, ACS Reagent) were all acquired from Sigma Aldrich (South Africa). All reagents were used without further purification.

2.2. Fabrication of catalysts

2.2.1. Synthesis of $BaTiO_3$ nanorods

The $BaTiO_3$ nanorods were synthesized using the solvothermal method described by Zhou et al. [26]. Initially, 9 mmol of polyvinylpyrrolidone was measured and dissolved in 25 mL of ethanol in a 100 mL flask, then stirred for 2 h at 30 ℃. After the surfactant was fully dissolved, 3 mmol of $C_{16}H_{36}O_4Ti$ solution was slowly added to the mixture while maintaining the temperature. Subsequently, 10 mL of 2 M KOH solution was introduced, forming a whitish slurry emulsion. Following this, 1 mmol of $Ba(OH)_2{\cdot}8H_2O$ was added to the emulsion and stirred for a few minutes before being transferred into a 100 mL Teflon-lined autoclave and heated at 200 ℃ for 2 hours. The resulting products were collected by centrifugation and washed three times each with 0.1 mol formic acid and deionized water. Finally, the washed precipitates were dried in an oven at 105 ℃ and calcined in a muffle furnace at 800 ℃ for 3 hours in the atmosphere

2.2.2. Preparation of $BaTiO_3/Cd_{0.5}Zn_{0.5}S$ heterojunction

A facile solvothermal synthesis technique was used to prepare the $BaTiO_3/Cd_{0.5}Zn_{0.5}S$ (1.0BTO/CZS) (Scheme 1) [44]. Briefly, 10 mmol of Cd^{2+}, Zn^{2+}, and the fabricated BTO were dissolved in 40 mL ethylene glycol and stirred for 10 min. NaOH (40 mmol) was added to the above mixture with continuous stirring. Subsequently, 25 mmol thioacetamide was added to the mixture with further stirring for 30 min, and then the mixture was transferred into a Teflon-lined autoclave and heated at 180 ℃ for 24 hours. The mixture was left to cool to room temperature, and then the yellowish powder (precipitate) was collected via centrifugation and washed several times with deionized water and absolute ethanol. The composite powder was dried overnight at 60 ℃ an oven; it was marked 1.0BTO/CZS (1:1 mol ratios). Different mass ratios were optimized to further elucidate interfacial contact, charge transfer, charge separation, and piezo-photocatalytic performance. This allows the fine-tuning of electronic properties and structural properties of the

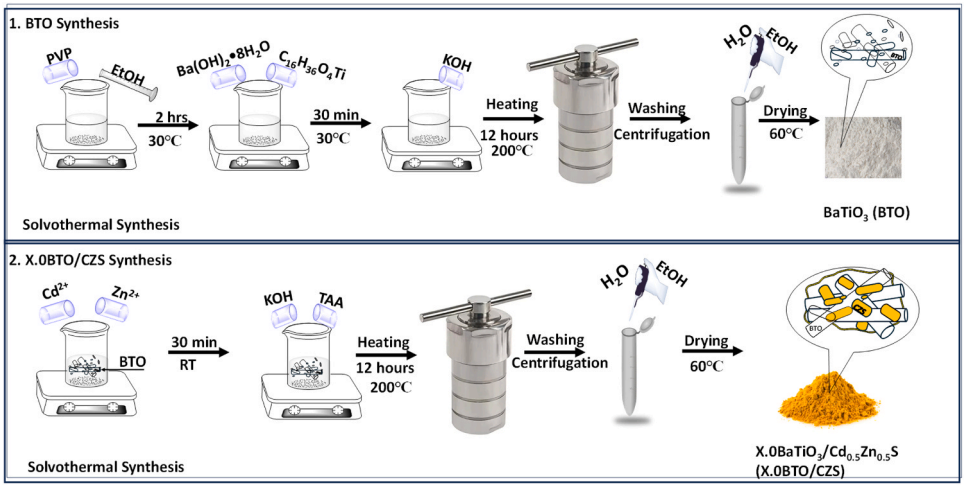

Scheme 1. Fabrication of pristine BTO and composite X.0BTO/CZS using the solvothermal method.

composite heterostructure. Different ratios of the heterostructure were fabricated using the same procedure by varying the ratios of CZS to BTO and labelled 2.0BTO/CZS (2:1 mol ratio) and 4.0BTO/CZS (4:1 mol ratio), respectively, and the pristine CZS was synthesized without the addition of BTO.

2.3. Characterization

X-ray diffraction (XRD, Advanced XRD diffractometer with Cu Kα radiation (λ = 154.18 pm)) was employed to analyze the materials. The surface morphology of the samples was observed using scanning electron microscopy (SEM, VEGA 3 TESCAN software, Czech Republic), and the internal morphology and crystallinity of the nanostructures was studied using transmission electron microscopy (TEM, JEM-2100, JEOL, Japan). The chemical composition and the sample states were characterized using X-ray photoelectron spectroscopy (XPS, Thermo ESCAlab 250Xi). The optical properties of the catalysts were analyzed using UV–visible diffraction spectroscopy (UV-Vis DRS, Agilent, USA, Cary60). The specific surface area, pore volume, and pore size were determined using the Brunauer-Emmett-Teller (BET, Micromeritics TriStar II, Germany). Charge transfer and recombination of the catalysts were analyzed using photoluminescence (PL, SHIMADZU RF-6000 Spectro-Fluorophotometer, Japan). Transient photocurrent response, linear sweep voltammetry (LSV), electrochemical impedance spectroscopy (EIS), and Mott-Schottky (M-S) were conducted using the Autolab electrochemical station with NOVA 2.1 software (Netherlands) with the 3-electrode system under visible light irradiation (70-watt solar lamp simulator, RSA). The blank electrode (reference) used was a 0.3 M Ag/AgCl electrode, and the platinum wire was employed as the counter electrode. The working electrode was fabricated by drop-casting the catalyst on the fluorine-doped tin oxide (FTO) substrate. Briefly, 50 mg of the catalysts, 5 wt% PVDF and 100 μ/mL NMP were thoroughly mixed to form a slurry. The slurry was applied on the conductive side of the FTO (1.5 cm×1.5 cm) and dried at 60 ℃ overnight. The electrolyte solution used for these analyses was 0.1 M sodium sulfate (Na_2SO_4) for LSV, transient photocurrent response (Bias potential = 1.5 V), and 5 mM $[Fe(CN)_6]^{3/4-}$ in 0.1 M KCl solution was used for EIS and M-S. The piezocurrent study was conducted using the three-electrode setup with 0.1 M Na_2SO_4 as the electrolyte. Ultrasonication power of 20-watt, with an amplitude of 20 %, was applied for 200 seconds with 10-second ON-OFF intervals. For the piezo-photocurrent study, the light source was kept on while the ultrasonicator was switched in intervals.

2.4. Piezo-photocatalytic evaluation

The piezo-photocatalytic performance of the catalyst was evaluated by assessing the concentration decay of CIP under ultrasonication and illumination conditions (Fig. S1). Typically, a controlled 500-watt ultrasonicator model VCX500 was used to provide external mechanical energy and an ice bath was used to maintain a constant temperature, while the 70-watt solar lamp provided light illumination. Firstly, 50 mg of the catalyst was dispersed into a 50 mL solution containing a concentration of 5 mgL^{-1} of CIP, and the solution was stirred for 30 min under dark conditions to achieve equilibrium. After that, ultrasonication (20-watt power) and illumination (70-watt solar lamp) were switched on for 90 continuous minutes, and 3 mL solution was collected every 15 min. The concentration decay and absorbance were analyzed using a Cary 60 UV-Vis spectrophotometer, and the mineralization of CIP was determined using total organic carbon (TOC) analysis. Synthetic and real water samples with the same pollutant degradation were used and analyzed using the Lotix QC03 TOC analyzer (Teledyne Tekmar, USA). The degradation and mineralization efficiency of the materials was evaluated using Eqs. (1) and (2):

$$\text{Percentage Degradation efficiency} = \frac{C_o - C_t}{C_o} x100 \quad (1)$$

$$\text{Percentage mineralization efficiency} = \frac{TOC_o - TOC_t}{TOC_o} \quad x \quad 100 \quad (2)$$

Here, C_0 and TOC_0 are the original concentrations at t = 0, and C_t and TOC_t are the concentrations at different time intervals. The analysis of the degradation products after piezo-photocatalytic degradation using 1.0BTO/CZS was performed using ultra-performance liquid chromatography-tandem to SYNAPT G1 mass spectrometer (UPLC-MS) (Waters, USA).

2.5. Determination of reactive species

The radicals responsible for piezo-photocatalytic oxidation of ciprofloxacin over 1.0BTO/CZS were determined by the trapping experiment. Specifically, 5 mmol of different trapping agents: tert-butanol (t-BuOH), acrylamide (AA), and sodium ethylenediamine tetraacetic acid disodium salt(EDTA-Na) into the system to trap the hydroxyl radicals ($^{\bullet}OH$), superoxides ($^{\bullet}O_2^-$), and holes (h^+), respectively.

3. Results and discussion

3.1. Structure and morphology

The phase structures of BTO, CZS, and 1.0BTO/CZS heterojunction were analyzed by XRD, shown in Fig. 1(a). The pristine BTO was observed to exhibit characteristic peaks at 21.9°, 25.1°, 31.2°, 38.6°, 44.9°, 50.5°, and 55.8° which corresponds to (100), (001), (110), 111), (200), (210), and (211) planes, respectively, indicating a cubic phase with high crystallinity (JCPDS: 04–016–4594, space group *Pm-3m*). CZS exhibit diffraction peaks at 25°, 26.6°, 28.4°, 36.9°, 44.3°, and 52.4° correspond to (100), (002), (101), (102), (101), (110), (103), and (200) planes which can be indexed as a hexagonal phase $Zn_{0.5}Cd_{0.5}S$ (JCPDS: 04–019–5121, space group *P6₃mc*). In the diffraction pattern of the 1.0BTO/CZS heterostructure, the peaks associated with both semiconductors are clearly seen, with some peaks merging at 45 ° and 55 °. It can also be seen that the crystallinity of the structure is maintained with only two foreign peaks detected, which can be attributed to the elements present in the precursor salts. Fig. 1(b) shows the Raman spectra of BTO, CZS, and 1.0BTO/CZS at room temperature in the visible region 100 and 800 cm^{-1}. For the pristine CZS, it was noted that there are two distinct peaks in the spectra corresponding to the 1LO and 2LO phonon modes of the $Cd_{0.5}Zn_{0.5}S$. The first peak at 307 cm^{-1} is assigned to the 1LO phonon mode, while the 614 cm^{-1} is assigned to the 2LO phonon mode. The existence of these phonon modes substantiates the high nanostructure crystallinity of the CZS. Pristine BTO spectra exhibited a sharp peak at 189 cm^{-1}, a broad band around 230 and 285 cm^{-1}, a small sharp peak at 343 cm-1, a broad peak at 415 cm^{-1} (B_1 g), 523 cm^{-1} (A1(3TO)), a shoulder peak at 587 cm^{-1}, a broad peak at 640 cm^{-1} (E_g), and small shoulder peak at 719 cm^{-1} (B1, E(LO +TO) & A1(LO)) [45]. The peaks at 189, 343, 523, and 640 cm^{-1} are associated with the cubic phase of the $BaTiO_3$ nanostructures [46]. Peaks near 190 and 516 cm^{-1} originate from the F1u mode of the cubic phase. Active peaks at 415 cm^{-1} suggest the presence of $BaCO_3$ in the pristine BTO, while 640 cm^{-1} indicates the presence of BTO nanostructures. Upon heterojunction formation, the peaks at 415 cm^{-1} were non-existent, indicating its removal and suppression. Raman spectra make it clear that the prepared nanostructures of BTO contain predominantly cubic-phase nanomaterials. The heterostructure (1.0BTO/CZS) also showed the integration of the CZS peaks with that of BTO, as highlighted. Most of the peaks of BTO can be detected in the spectra, indicating complete integration and fabrication of the 1.0BTO/CZS composite.

The field emission-scanning microscopy (FE-SEM) micrographs (Fig. 2(a–c)) show the pristine CZS, BTO, and composite 1.0BTO/CZS surface morphological structures. CZS exhibited thin nanorod-surface morphology with smooth surfaces, rounded edges, and fault stackings introduced by sulfur (Fig. 2(a)). Some spherical nanoparticles can be observed due to aggregation through the solvothermal process. BTO also showed nanorod surface morphology with a clear difference in width and length of said nanostructures compared to the CZS (Fig. 2(b)). The nanorod had thin, long grooves along the nanorod surface and seemingly flat edges. Fig. 2(c) shows the micrograph of the heterostructure (1.0BTO/CZS), indicating the presence of both the pristine nanostructures and the odd stacking that is linked to the presence of sulfur in the structure; there is an even distribution of both components based on the observable rod structures and identical aggregation, as seen with the pristine components. The heterostructure (1.0BTO/CZS) showed the formation of nanorods from both components, suggesting a balanced composition for the growth of nanorods of CZS due to optimized nucleation and interaction between BTO and CZS. There is a concentrated sulfur area with random arrangements of flake-like nanostructures, as shown by the elemental mapping micrographs of the heterostructure, confirming the presence of false stackings within the composite due to sulfur presence (Fig. S3). The presence of these elements in the composite was supported by energy dispersive spectroscopy (EDS) (Fig. 2(d)) and elemental mapping (Fig. S3). In contrast, ratios 2.0BTO/CZS (Fig. S3(a)) and 4.0BTO/CZS (Fig. S3(b)) exhibited only nanorods nanostructures from BTO and spherical-like nanomaterials from CZS with observable agglomeration. Excess BTO may have inhibited the growth of nanorods by limiting the self-assembly into nanorods of CZS due to low content (Fig. S4).

Transmission electron microscopy (TEM) analysis was conducted to investigate the microstructure of BTO, CZS, and the 1.0BTO/CZS composite (Fig. 2(a-c)). 1.0BTO/CZS micrographs revealed clusters of highly uniform nanorods with an average diameter of approximately 53.14 nm (Fig. S2). The presence of distinct lattice fringes (d-spacing of 0.9 nm) within the rods indicates high crystallinity, which is crucial for efficient electronic properties. This is consistent with observations reported by Rajendran and Vijayalakshmi [47] on the influence of NaOH in shaping BTO nanomaterials. The TEM image for $Cd_{0.5}Zn_{0.5}S$ (CZS) shows rod-like nanosheets, which are characteristic of this material. The rods appear to be well-defined with clear boundaries, indicating high crystallinity (Fig. 3(b)). Interestingly, the TEM image of the 1.0BTO/CZS composite (Fig. 3(c)) showcased a unique heterostructure morphology. BTO nanorods appeared coated with thin, stacked nanosheets, potentially indicating the presence of mild fault stackings within the structure. These faults could be vacancies introduced by the incorporation of sulfur. Notably, lattice fringes were also observed in the composite, signifying the high crystallinity maintained even after integrating the BTO nanomaterial. These observations strongly support the successful

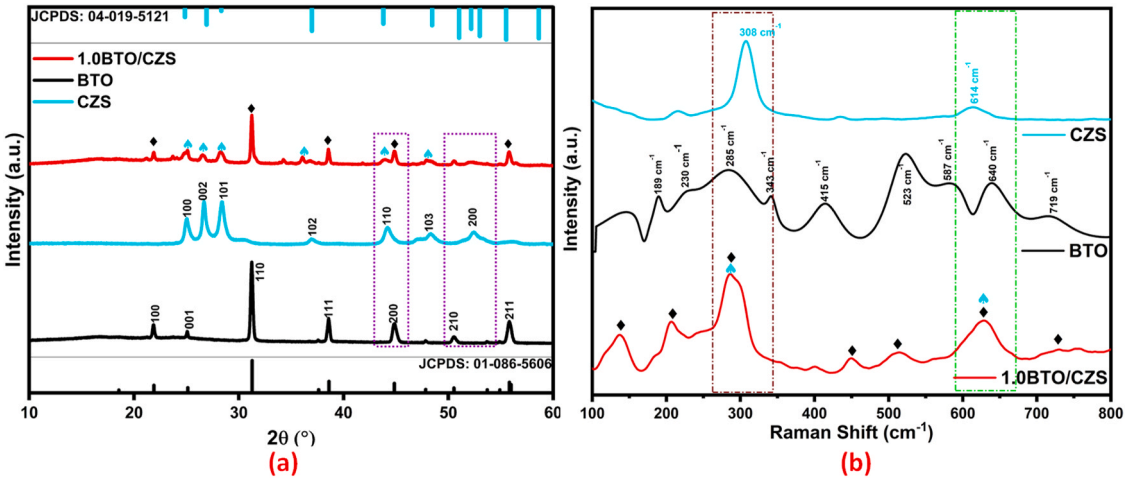

Fig. 1. (a) XRD pattern and (b) Raman spectra of as-prepared BTO, CZS, and 1.0BTO/CZS.

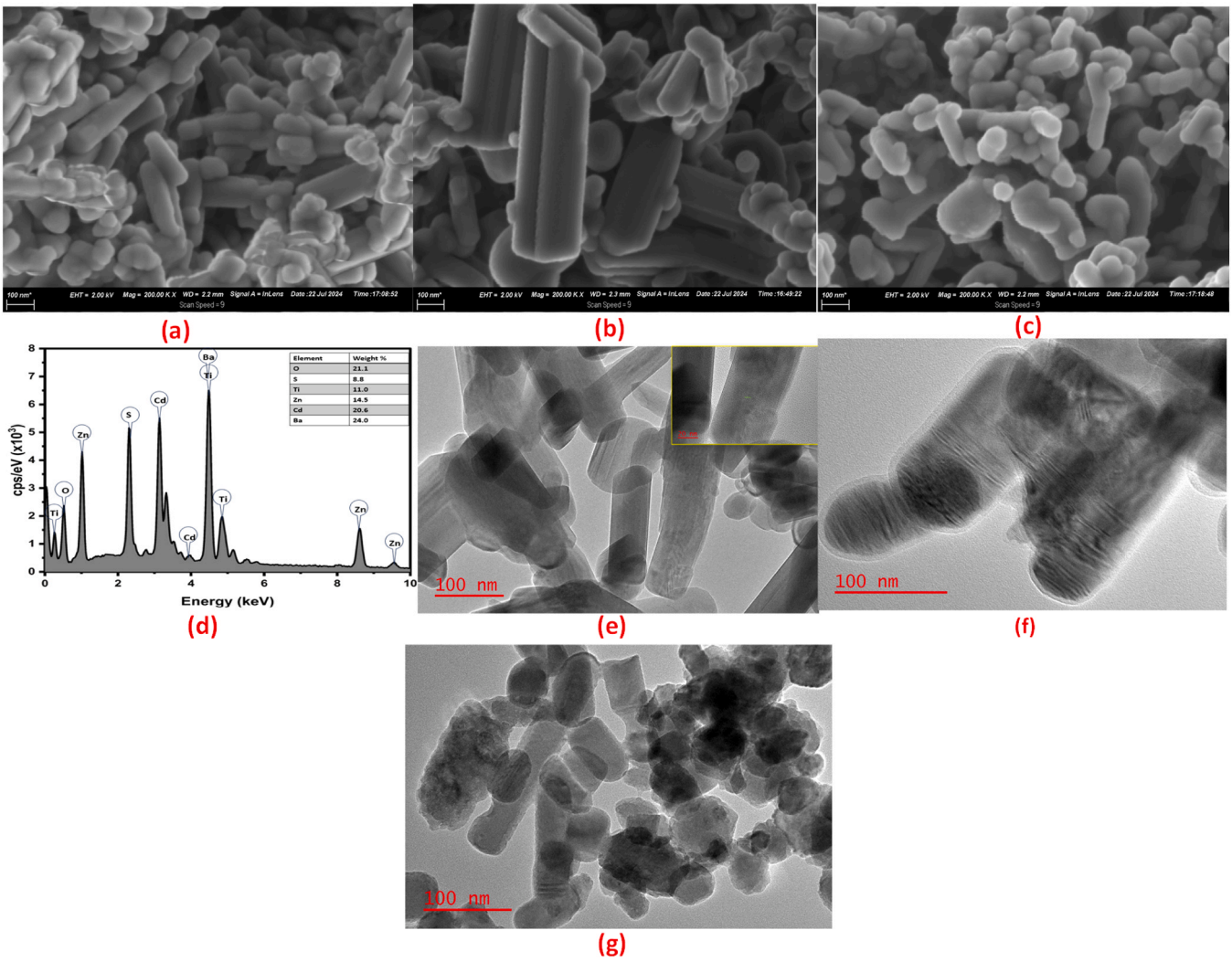

Fig. 2. FE-SEM mages of the as-prepared nanomaterials, (a) CZS), (b) BTO, (c) 1.0BTO/CZS, (d) EDS analysis of 1.0BTO/CZS, TEM micrographs of (e) BTO (insert x20 nm BTO), (f) CZS, and (g) 1.0BTO/CZS.

formation of the 1.0BTO/CZS heterostructure.

The N_2 adsorption-desorption isotherms (Fig. 3(a-c)) were employed to assess the surface area, pore size distribution, and pore volume of BTO, CZS, and 1.0BTO/CZS samples. All materials exhibited type IV isotherms with a characteristic H3 hysteresis loop, indicative of a mesoporous and macroporous structure because of stacking due to their 1-D structure. The pristine CZS possessed the highest Brunauer-Emmett-Teller (BET) surface area (45.649 m^2/g) compared to pristine BTO (7.509 m^2/g). Notably, the 1.0BTO/CZS composite exhibited a BET surface area of 32.507 m^2/g, suggesting a significant contribution from the inherent porosity of CZS. This porosity in CZS is further corroborated by its larger pore volume (0.29 cm^3/g) compared to BTO (0.03 cm^3/g) (Table 1), likely arising from sulfur-induced fault stacking within its crystal structure. Fig. 3(d-f) depicts the pore size and volume distribution profiles for all three materials. The Langmuir isotherm of the other fabricated ratios is shown in Fig. S5, indicating a type IV isotherm and H3 hysteresis loops. Ratio 2.0BTO/CZS and 4.0BTO both exhibited the lowest BET surface areas compared to 1.0BTO/CZS with SA of 9.642 m^2/g and 9.0024 m^2/g, respectively. All samples displayed a dominant pore size range between 0 and 20 nm. However, CZS exhibited a broader distribution with larger pores exceeding 135.94 nm, whereas BTO primarily possessed pores around 147.38 nm. Interestingly, the 1.0BTO/CZS composite showcased a reduction in the dominance of large pores from CZS while achieving a desirable average pore size of approximately 137.99 nm. This composite also retained a significant concentration of pores above 20 nm and maintained a total pore volume of 0.14 cm^3 /g. The observed pore size distribution of the 1.0BTO/CZS composite suggests the presence of both meso- and macropores. The smaller pores (0–20 nm) contribute to a high surface area, facilitating efficient pollutant adsorption. Conversely, the larger pores (>20 nm) enable deeper penetration of pollutants into the active sites within the material. Within the 1.0BTO/CZS ratio, there is a uniform distribution of mesopores (pore sizes), which is good for adsorption, and the same can be observed in the bare samples indicated by the BJH and BET pore size difference (Table S1). The ratio 2.0BTO/CZS and 4.0BTO/CZS, however, indicated a discrepancy in terms of BET pore sizes and BJH pore sizes, indicating an uneven pore size and distribution, which can be due to poor nucleation of the nanorods as observed in 1.0BTO/CZS leading to lower adsorption. This combination, potentially driven by capillary action rather than solely surface adsorption, is hypothesized to be a key factor in the enhanced catalytic performance of the 1.0BTO/CZS composite. This data also reinforces that piezocatalysis mainly stems from efficient charge transfer and oxidant generation rather than being dependent on the surface area.

3.2. XPS analysis

The chemical and surface electron states of the elements in the

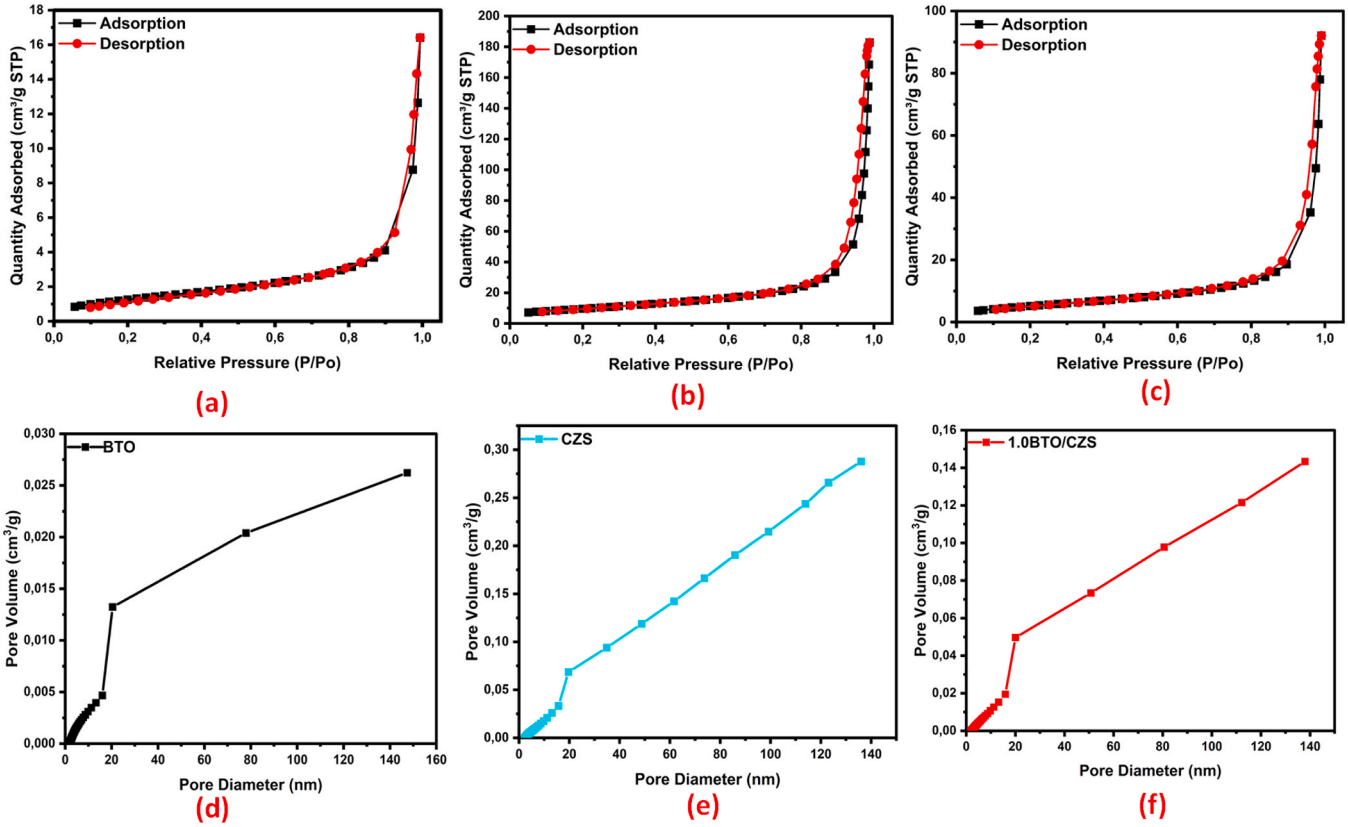

Fig. 3. Pore structure analysis of the BTO, CZS, and 1.0BTO/CZS. (a-c) N_2 Adsorption-desorption isotherms and (d-f) pore size and volume distribution plots.

Table 1
BET surface area, BJH adsorption pore size distribution, and pore volume.

Sample	Surface Area (m^2/g)	Average Pore Diameter (nm)	Average Pore Volume (cm^3/g)
BTO	4.8118	147.38	0.03
CZS	35.1617	135.94	0.29
1.0BTO/CZS	19.4868	137.99	0.14

catalysts were assessed by XPS analysis. As shown in Fig. 5(a), the survey spectra indicate that the composite heterostructure is composed of Ba, Ti, O, Cd, Zn, and S. The high-resolution spectrum of the Cd element is shown in Fig. 4(b). There are two distinct peaks, with one attributed to Cd $3d_{5/2}$ bonded to oxygen (O) and sulfur. In the pristine CZS, the Cd peak is at position 404.8 eV, which redshifts to 404.9 eV (higher binding energy), indicating loss of electrons donating them to sulfur. Fig. 5(c) displays signals at 1021.7 eV and 1044.8 eV belonging to Zn 2p (Zn $2p_{1/2}$ and Zn $2p_{3/2}$) in the pristine CZS. In the composite heterostructure (1.0BTO/CZS), the peak assigned to the Zn-S bond shifts to a lower binding energy of 1021.6 eV from 1021.7 eV, showing the gaining of electrons from sulfur [48]. The deconvolution of XPS of sulfur in CZS is fitted in Fig. 5(d) for S 2p with binding energies of 161.5 and 162.2 eV (S $2p_{3/2}$ and S $2p_{1/2}$), signifying a sulfur doublet. A noticeable shift in the binding energy of $S_{3/2}$ was observed in the composite from 161.5 eV to 161.3 eV, and that of S $2p_{1/2}$ shifted from 162.2 eV to 162.4 eV, indicating a decrease in the electron density. Positive shifts in sulfur (S $2p_{3/2}$) are commonly attributed to an oxidized state, which can be a result of structural defects and sulfur vacancies in the structure or interaction with oxygen as it is more electronegative [49].

The Ba showed distinct peaks for BTO fitted at 778.8, 780.4 eV, and 794 eV belonging to Ba $3d_{5/2}$ and Ba $3d_{3/2}$, respectively (Fig. 4**(e)**). The peak at 778.8 eV (Ba $3d_{3/2}$) is attributed to the interaction of Ba with O (forming BaO) and O_2 (forming BaO_2), which also causes blueshifts in the heterostructure to 778.7 eV for BaO and 780.1 eV for BaO_2, and the redshift of Ba $3d_{3/2}$ down to 793.9 eV, respectively. As depicted in Fig. 4 **(f)**, the peaks Ti $2p_{3/2}$ are found at 457.9 eV in the pristine state, while in the composite heterostructure, it is fitted at 458.1 eV, indicating a blue shift due to a reduction in the electron density. However, peak Ti $2p_{1/2}$ blueshifts by 0.1 eV in the heterostructure, and the peak is attributed to the interaction of Ti with oxygen in both the BTO and 1.0BTO/CZS structure. The O 1 s spectrum is illustrated in Fig. 5(g) BTO and 1.0BTO/CZS, indicating three (3) peaks assigned to metal oxide (M-O, lattice oxygen), chemisorbed oxygen (C-O, hydroxyls), and adsorbed water (C═O, physically adsorbed oxygen) interactions [48]. The binding energy of the M-O (lattice oxygen) shifted from 529.1 eV (BTO) to 529.6 eV (1.0BTO/CZS), indicating a change in the structure during heterostructure formation. A higher binding energy shift of the M-O also indicates Ba losing electrons to the oxygen, reaching higher oxidation states. This creates a stronger bond between the metal and the oxygen, altering and enhancing the catalytic activity, conductivity, and stability of the heterostructure and providing more active sites for adsorption. The bonds C-O (hydroxyls) and C═O can be observed in the range of 530.8–531.7 eV and 532.5–533.3 eV for all the materials, which could be the result of adventitious hydroxyls that can be introduced by water vapor on the surface of the material in ambient temperatures.

3.3. Optical and photoelectrochemical properties

A desired property of a good photocatalyst is the ability to absorb light in a wide range of the solar spectrum, ideally extending from the ultraviolet to the visible region. To investigate the light absorption property of these materials, ultraviolet-visible diffuse reflection spectra (UV–vis DRS) were utilized. As shown in Fig. 5(a), the absorption edges of BTO, CZS, 1.0BTO/CZS, 2.0BTO/CZS, and 4.0BTO/CZS are 405 nm, 544 nm, 567 nm, 578 nm, and 555 nm, respectively. Thus, the

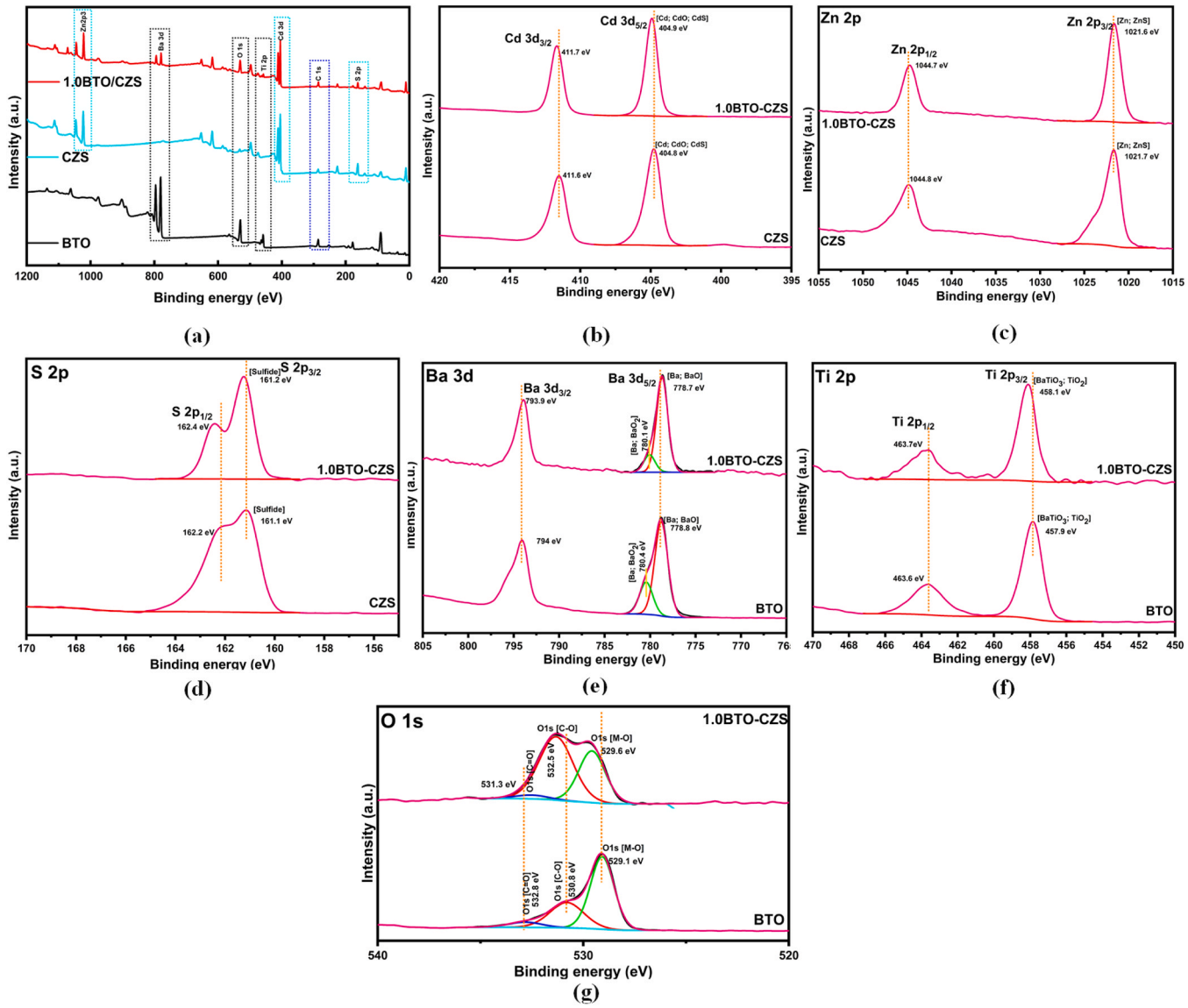

Fig. 4. XPS-high resolution of BTO, CZS, and 1.0BTO/CZS, (a) survey spectra, (b) Cd 3d, (c) Zn 2p, (d) S 2p, (e) Ba 3d, (f) Ti 2p, and g) O 1 s.

deposition of CZS on BTO improved the light absorption capacity of the heterostructure, as shown by the increased absorption wavelength. The bandgap energies of the materials were determined using Tauc plots (Fig. 5(b)). The bandgap values for the pristine nanomaterials were calculated to be 2.87 eV for BTO and 2.20 eV for CZS. For the heterostructures, the band gaps were found to be 2.03 eV for 4.0BTO/CZS, 1.89 eV for 2.0BTO/CZS, and 1.85 eV for 1.0BTO/CZS. A narrower band complements the spectrum, providing a higher absorption capacity of 1.0BTO/CZS.

The Mott-Schottky plots (Fig. 5(c)) for both CZS and BTO show positive slopes for both CZS and BTO, indicating the n-type behavior of the semiconductors. The extrapolated x-intercept represents the flat band (E_{FB}) potential, equivalent to the nanomaterial's fermi energy (E_F) level. The E_{FB} was determined to be −0.94 V and −0.52 V for CZS and BTO, respectively. The reported potentials are in Ag/AgCl, and the conversion was done using the Nernst equation into a normal hydrogen electrode (NHE) [50,51].

$$E_{FB}\ (\text{vs. NHE}) = E_{FB}\ (\text{vs. Ag/AgCl}) + E_{Ag/AgCl} + 0.059\text{xpH} \quad (3)$$

Where is $E_{Ag/AgCl}$ 0.197 V at 25 ℃, and the pH of the electrolyte was measured to be 6.5. The newly converted E_{FB} are 0.060 V and −0.359 V vs NHE for BTO and CZS, respectively. It has been reported that the conduction band (E_{CB}) is 0.1–0.3 V above the Fermi energy level for n-type nanomaterials. Thus, the calculated conduction band (E_{CB}) of BTO is determined to be −0.24 V, that of CZS was determined to be −0.659 V vs. NHE, and the valence band (E_{CB}) for BTO and CZS were determined using the equation:

$$E_{VB} = E_{CB} + E_g \quad (4)$$

The valence band (E_{VB}) was calculated to be 2.63 V for BTO and 1.54 V vs NHE for CZS. The energy band structure of CZS and BTO is shown in Fig. 5(d). The valence band maxima (VBM) were analyzed using XPS, and it was determined to be 0.49 eV and 1.78 eV for CZS and BTO, respectively (Fig. S6). Additionally, the MS plots were utilized in the estimation of charge carrier density (concentration) (ND, donor carriers of n-type semiconductors) for fabricated nanostructures, using Eq. (5):

$$N_D = \frac{2}{e\varepsilon\varepsilon_0 X\ \text{Slope}} \quad (5)$$

Where e, ε, and ε_0 represents the electron charge, dielectric constant, and vacuum permittivity, respectively. The dielectric constants of CZS

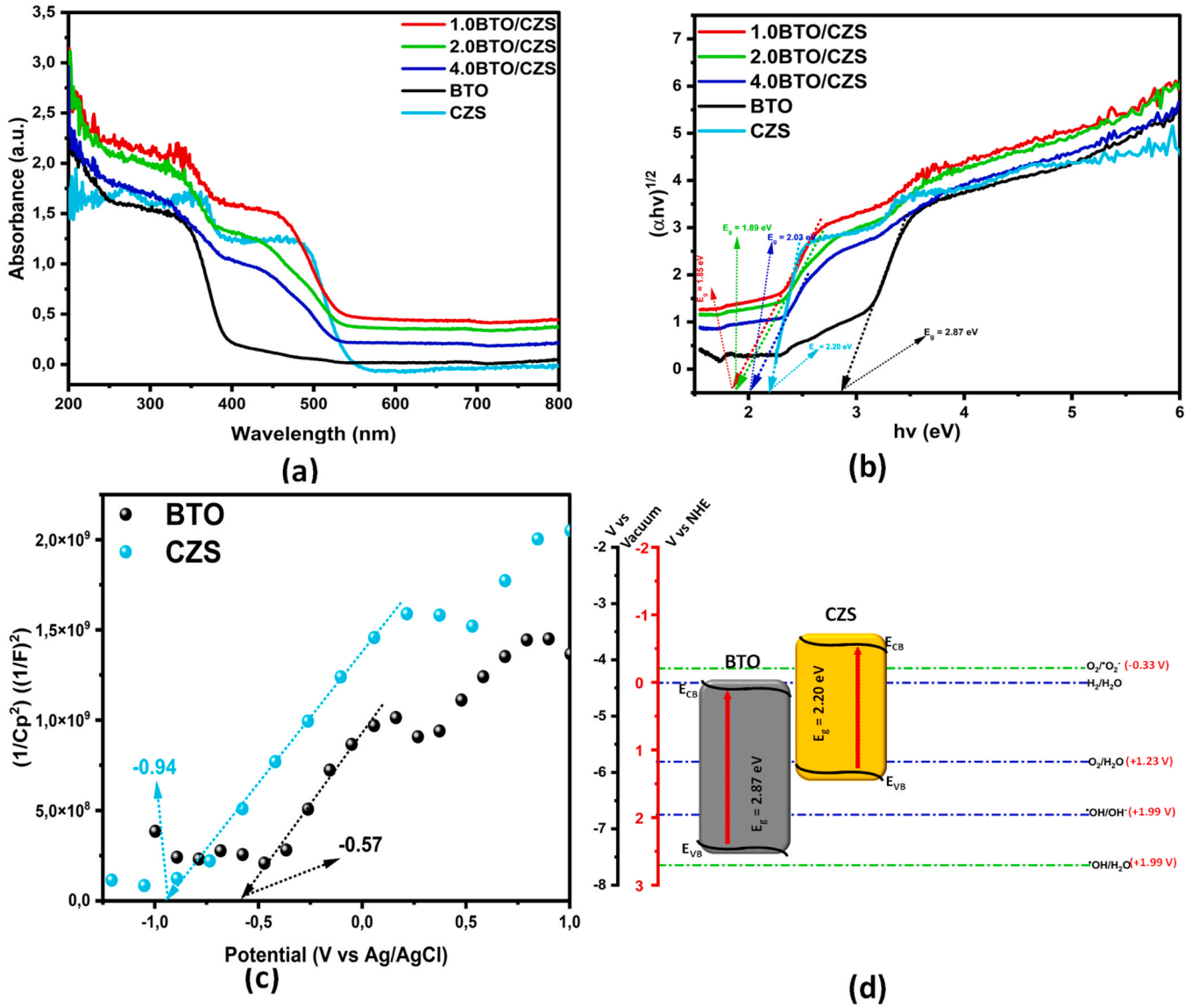

Fig. 5. (a) UV–vis diffraction spectrum, (b) Tauc plots, (c) Mott-Schottky of BTO and CZS, and (d) Band edge diagram of CZS and BTO.

were estimated from its binary sulfides (ZnS, CdS), where CdS is around 8.9 [52], and ZnS is about 8.37 [53]. The approximate dielectric constant of $Cd_{0.5}Zn_{0.5}S$ is 8.64. In terms of BTO, the dielectric constant of the tetragonal phase reaches a maximum of ~500. The calculated N_D from each slope is estimated to be 3.01×1023, 5.54×1021, 9.54×1021, 7.20×1021, and $2.13 \times 1021\ cm^{-3}$ for CZS, BTO, 1.0BTO/CZS, 2.0BTO/CZS, and 4.0BTO/CZS, respectively. CZS had the lowest slope and the highest ND, highlighting an inverse relationship between the MS slope and ND, where the increase in slope results in the lowest charge carrier density.

Obtained work functions of CZs and BTO are shown in Fig. 6, where they were obtained via XPS, and sketches of the internal electric field and charger transfer are highlighted. The relationship of the solid sample provides the energy transformation in the XPS measurement using the Eq. (6):

$$h\nu = E_k + E_b + \Phi \tag{6}$$

Where $h\nu$ is the incident photon energy, E_k is the photon electron energy, E_b is the electron binding energy, and Φ represents the sample's work function [54]. The difference in work function creates a contact potential difference (ΔV), which can be calculated using Eq. (7):

$$\Delta V = \Phi - \varphi \tag{7}$$

Where φ is the work function of the instrument with the value of 5.05 eV, this alters the kinetic energy of free electrons, which in turn changes their binding energy. By measuring the distance between the inflection points (IP), the potential difference can be determined, leading to the calculation of Φ (Fig. 6(a–b)). The calculated work functions of CZS and BTO were determined to be 6.851 eV and 7.534 eV, respectively. Fig. 6(c) shows the estimated band edges (Fig. 6) (VB and CB), work functions, and fermi energy levels. This arrangement substantiates the existence of S-Scheme between BTO and CZS in the heterojunction composite.

The transient photocurrent responses of the materials were analyzed at 10-second intervals during ON-OFF cycles of solar lamp irradiation using chronoamperometry with a 1.5 V applied potential. (Fig. 7(a)). These responses provided the information to evaluate the transfer of photoinduced carriers and photocatalytic performance of the pristine materials and heterostructures. BTO and CZS show a maximum photocurrent response of 0.005 and 0.176 mA/cm^2, respectively. While the fabricated heterostructures show a much higher response (Table S2). The combination of CZS and BTO proved to enhance carrier separation

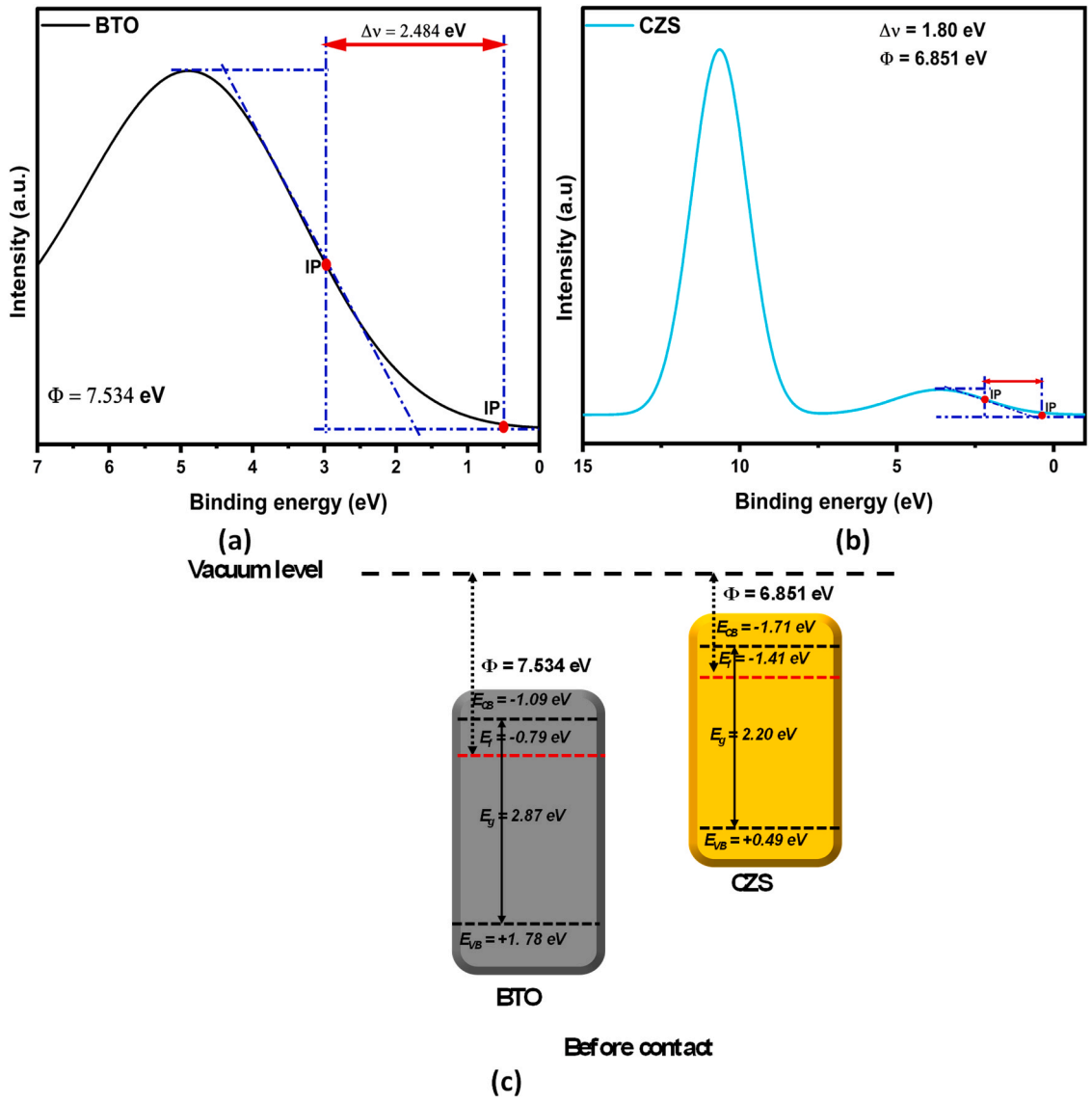

Fig. 6. (a-b) Work function of all the fabricated pristine nanostructures measured by VB XPS and (c) electron migration to reach vacuum.

and acceleration of charge transfer on the catalyst surface, with 1.0BTO/CZS having a much higher response that is ~13,5 times that of BTO and ~3 times than that of CZS with a recorded maximum of 0.27 mA/cm^2. Linear sweep voltammetry(LSV) was further used to complement the photocurrent response. Based on the LSV curves (Fig. 7(b)), the 1.0BTO/CZS heterostructure exhibits the highest current density of 9.47 mA/cm^2, which was observed at the anodic vertex of 2.00 V conditions. High current density responses correlate to enhanced catalytic activity of nanostructures, and it can be observed that CZS had a higher density compared to BTO, which the improvement can be attributed to. Electrochemical impedance spectroscopy (EIS) was employed to investigate charge transport capabilities by analyzing the Nyquist plots fitted using the Randles circuit (Fig. S7). As shown in Fig. 7(c), 1.0BTO/CZS exhibited the smallest arc radius compared to other ratios, indicating the lowest charge transfer resistance. This suggests enhanced charge transfer potential and improved charge separation under light illumination. The heterostructure formation between BTO and CZS modified electron transport and migration between the two semiconductors (Table S3). CZS with a negative conduction band energy means that it tends to donate electrons when excited by light, facilitating charge separation and potentially participating in redox reactions.

Photoluminescence (PL) analysis was employed for the investigation of the charge carrier dynamics and the efficiency of electron-hole separation of the materials. As shown in Fig. 7(d), the emission spectra of all the materials have a fluorescence peak at 390 nm. Notably, the rate of electron-hole recombination is indicated by the intensity of the peak, with a lower indicating an improved charge recombination rate. Among the heterostructures, 1.0BTO/CZS demonstrated a prolonged charge carrier lifetime, indicated by its lower PL intensity compared to 2.0BTO/CZS and 4.0BTO/CZS. This reduced PL intensity suggests that electrons lose energy and return to the valence band less frequently, implying superior photocatalytic activity under light irradiation for 1.0BTO/CZS. The fluorescence peak for pure CZS falls between those of the composites and pure BTO, indicating better performance than pristine BTO, which further justifies its selection as a component catalyst in the heterostructure formation.

Electrochemical impedance spectroscopy (EIS) under ultrasonication, illumination, and the combination was conducted for all the synthesized nanostructures (BTO, CZS, 1.0BTO/CZS, 2.0BTO/CZS, and 4.0BTO/CZS) (Fig. 8(a–b)). Nyquist plots obtained from the fabricated nanomaterial highlighted that under ultrasonication only, BTO had the smallest charge transfer resistance while CZS had the highest Rct, slightly above 4.0BTO/CZS. Surprisingly, 2.0BTO/CZS had the highest Rct, and 1.0BTO/CZS had the second highest Rct, indicating that pure

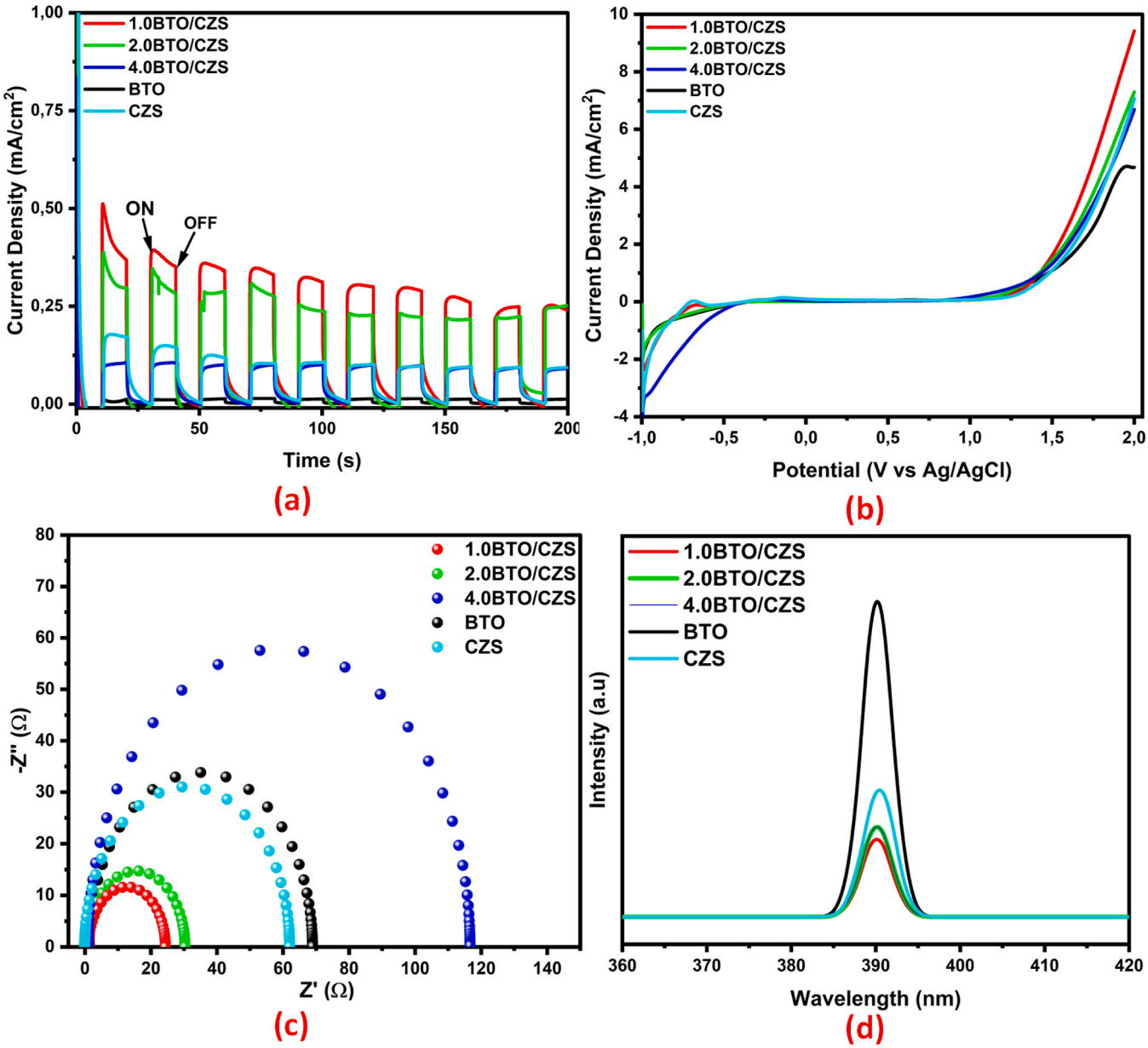

Fig. 7. (a) Transient photocurrent response, (b) Linear sweep voltammetry, (c) Nyquist plots, and (d) PL of synthesized BTO, CZS, 1.0BTO/CZS, 2.0BTO/CZS, and 4.0BTO/CZS.

BTO performs better than CZS under ultrasonication. When ultrasonication and illumination were used together for excitation, ratio 1.0BTO/CZS had the smallest Rct, showing the best synergy for charge transfer between the nanorods-based composite. Smaller Rct shows good optimization and interaction between BTO and CZS, which is necessary for maximum efficiency. 2.0BTO/CZS had the second smallest Rct under both illumination and ultrasonication, showing a positive linear relationship with the increase in mole ratio of CZS.

Transient piezocurrent and piezo-photocurrent response of the catalyst were investigated at intervals of 10 seconds ON-OFF cycle of the ultrasonicator while light illumination was kept constant for 200 seconds. Fig. 8(c) shows a comparison of photocurrent response, piezocurrent response, and piezo-photocurrent response. The piezocurrent response of both the pristine and heterostructures showed a similar response, while 1.0BTO/CZS and 2.0BTO/CZS had the same maximum current density response of 0.11 mA/cm^2, BTO and 4.0BTO/CZS had the same current density of 0.08 mA/cm^2. Higher ratios of CZS in the material correlate with a stronger piezocurrent response due to its inherent piezoelectricity, arising from the 1D nanostructure morphology and the non-centrosymmetric *P6₃mc* space group [55]. This configuration is common in materials that exhibit piezoelectric and ferroelectric properties due to their non-centrosymmetric nature. The combination of both ultrasonication and constant light illumination indicated that the pattern in transient photocurrent response is identical to that in piezo-photocurrent response. 1.0BTO/CZS had the highest response due to the application of ultrasonication every 10 seconds, which was double that of photocurrent and 6 times that of the piezocurrent response. This substantiates that the heterostructure has an improved piezo-photocatalytic activity due to significantly enhanced due to improved charge carrier separation induced by the internal electric field. The BTO provides mainly the piezoelectric properties in the heterostructure, while CZS provides both piezo- and photocatalytic properties, enhancing the performance of the catalyst. This study further demonstrates a strong synergistic effect in combining piezocatalysis and photocatalysis, proving them to be potent solutions for environmental challenges.

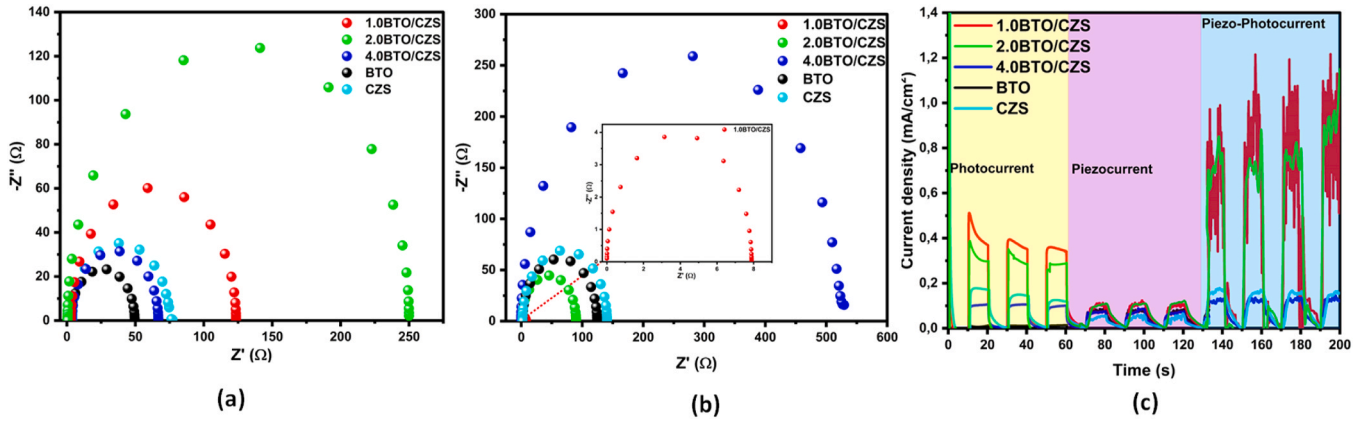

Fig. 8. Electrochemical impedance spectroscopy (EIS) under (a) ultrasound, (b) ultrasound + light, (c) Transient photocurrent, piezocurrent, and piezo-photocurrent response of materials (CZS, BTO, 1.0BTO/CZS, 2.0BTO/CZS, and 4.0BTO/CZS).

3.4. Piezo-photocatalytic degradation of ciprofloxacin

The piezo-photocatalytic activity of the ratios BTO/CZS (1.0BTO/CZS, 2.0BTO/CZS, and 4.0BTO/CZS) was assessed towards the degradation of ciprofloxacin under light illumination and constant ultrasonication (Fig. 9(a–b)). 1.0BTO/CZS heterostructure exhibits the highest catalytic performance because of the piezo-photonic effect brought by the induced polarization charges as indicated for the degradation of CIP under combined ultrasonication and illumination sources for piezo-photocatalysis. Noticeably, the dark adsorption of the CIP for 30 min was also higher for 1.0BTO/CZS compared to the ratio 2.0BTO/CZS and 4.0BTO/CZS, highlighting a multifunctional system of adsorption and degradation as shown by the deep drop in concentration between 0 and 30 min. A similar observation was made for the ratio 2.0BTO/CZS. Enhanced electrochemical properties and piezo-photocatalytic properties of 1.0BTO/CZS can be attributed to the morphology of the nanorod combination that allows for an even distribution of mechanical stress, increased active sites introduced by the sulfur defects, and a direct pathway for charge carriers. The adsorption efficiency of the composite heterostructures is highlighted in Fig. S8 between 15 min and 30 min of dark adsorption-desorption equilibrium. The heterostructure (1.0BTO/CZS) also showed a higher catalytic performance than BTO and CZS, reaching a degradation efficiency of ~85 %, which is 2–3 times that of its components by monitoring the concentration decay (Fig. 9(c)) and the absorption maxima of CIP at *ca.* 278 nm (Fig. S9). Notably, ~50 % of the ciprofloxacin was adsorbed during the initial dark equilibrium period (0–30 min), prior to initiating the piezo-photocatalytic reaction. This indicates that ~60 % of the remaining pollutant was degraded by the catalyst under illumination and ultrasonication. The high initial adsorption is attributed to the meso- and macroporous structure of 1.0BTO/CZS (see Fig. 3), along with sulfur-induced defect sites that increase the number of available active adsorption sites. The synergistic effect of combining photocatalysis and piezocatalysis was investigated by examining the degradation performance of each process. Photocatalysis and piezocatalysis alone achieved degradation rates of 31.5 % and 59.2 %, respectively (Fig. 9(d-e)). There is a deep concentration decay of CIP at 60–75-minute intervals, which is the result of delayed catalyst complete activation, gradual adsorption, and degradation of adsorbed intermediates when the radical pool reaches its maximum. During the individual piezocatalytic process, the concentration spike, which could be the result of early desorption or a reaction between intermediates having the same light absorbance wavelength. Evaluating the efficiency between the pristine nanostructures and the composite for piezocatalysis, photocatalysis, and the hybrid process (piezo-photocatalysis) highlighted that the heterostructure outperformed the bare materials in all three (3) processes, with the largest contributor being photocatalysis (Fig. 9(f)).

The synergy between the piezocatalytic and photocatalytic components of the hybrid process was evaluated using Eq. (8 & 9).

$$\text{Synergy factor} = \frac{k_{app}(Piezo - Photo)}{k_{app(Piezo+Photo)}} \tag{8}$$

$$\%Synergy = \frac{k_{app}(Piezo - Photo) - k_{app}(Piezo + Photo)}{k_{app(Piezo-Photo)}} \; x \; 100 \tag{9}$$

The synergy factor and the synergy percentage were determined to be 1.3 and 23 %, respectively. This indicates the synergistic effect of piezo-photocatalysis in the presence of 1.0BTO/CZS in the degradation process. Piezocatalysis can actively increase photocatalytic performance, as shown by the great increase in efficiency when ultrasonication was introduced for 90 min under 20 W and 45 KJ of energy applied (Fig. 9(a-b)). Compared to previously reported $BaTiO_3$ heterojunctions for piezo-photocatalytic degradation of organic pollutants, 1.0BTO/CZS exhibited outstanding performance with minimal energy requirements, such as lower ultrasonication power, light intensity, and catalyst dosage (Table 2). The oxidation of CIP was also investigated by subjecting the analyte to piezolysis and photolysis without a catalyst. The results showed minimal reduction in analyte concentration, achieving only 2 % and 5.87 %, respectively. Piezocatalysis, photocatalysis, and piezo-photocatalysis degradation rates were quantitatively using Eqs. (10) and (11), as shown in Fig. 9(c), with the *k*-values of each process compared.

$$\ln\frac{C_0}{C_t} = k_1 t \tag{10}$$

For the pseudo-second-order model plot, the data was obtained from Eq. (6) as:

$$\frac{1}{C_t} - \frac{1}{C_0} = k_2 t \tag{11}$$

Where C_0 (mgL^{-1}) and C_t are the initial and final concentrations of CIP at a certain time, t (min), and *k* is the rate constant. The 1.0BTO/CZS heterostructure had a higher *k* value of 0.01239 min^{-1} for piezo-photocatalysis, while pure BTO and CZS had *k* values of 0.00453 min^{-1} and 0.00252 min^{-1}, respectively (Fig. 9(f)) for first order kinetics. The rate constant of the piezo-photocatalysis is 2 times that of photocatalysis and ~3.7 times that of piezocatalysis. The efficiency of the heterostructure was further evaluated by applying pristine materials in photocatalysis and piezocatalysis processes (Fig. 9(d)). Pristine CZS showed comparable photocatalytic performance with 1.0BTO/CZS but poor piezocatalytic performance. BTO showed almost the same performance in all the degradation processes. However, the

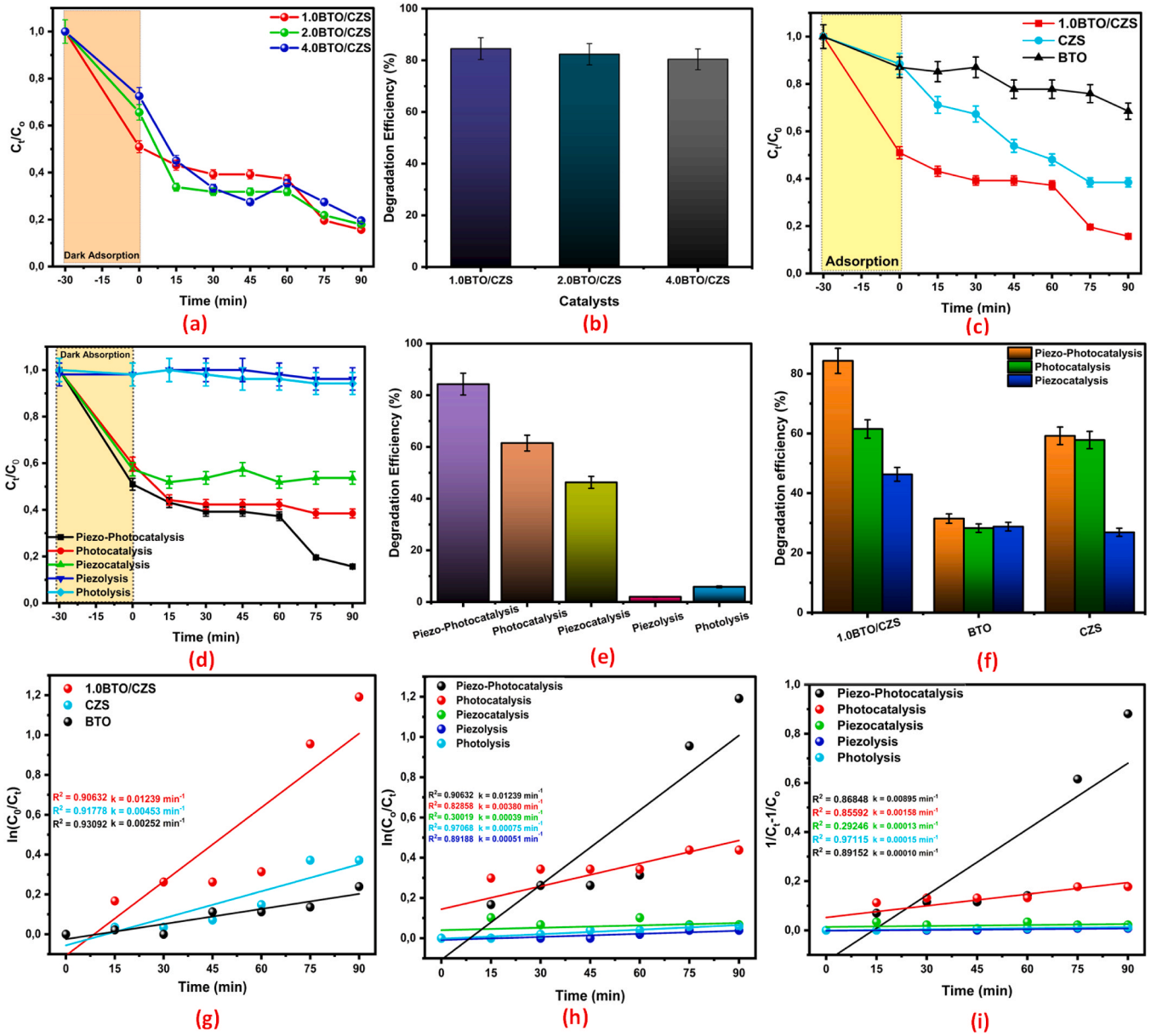

Fig. 9. Degradation efficiencies of (a-b) BTO/CZS ratios, (c) piezo-photocatalysis of 1.0BTO/CZS, CZS, and BTO, (d-e) piezocatalysis, piezolysis, photocatalysis, photolysis, and piezo-photocatalysis, and their corresponding nano, (f) Comparative degradation studies (BTO, CZS, and 1.0BTO/CZS), and (g) kinetic curves for comparative studies, (h) pseudo-first order, and (i) pseudo-second-order kinetics.

Table 2
Comparative performance of various heterojunction-based catalysts for the removal of organic pollutants.

Catalyst	Organic Pollutant	Reaction Conditions	Time	%Degradation Efficiency	Ref.
$BaTiO_3/La_2Ti_2O$	CIP	300 W Xenon lamp + 210 W 40 kHz	90 Min	50.2	[56]
$FTO/BaTiO_3/SnO_2$	CIP	40 kHz Ultrasonic + 100 W Xe lamp	180 Min	94	[57]
$BaTiO_3/CuPbSbS_3$	RhB	100 W 40 kHz Ultrasonicator, 300 W Solar Simulator	60 Min	90.5 %	[32]
$FTO/BaTiO_3/AgNPs$	CIP (5 mg/L)	24 kHz ultrasonicator, 70 W Solar light	180 Min	72 %	[58]
$BaTiO_3/0.8CuO$	MO (10 mg/L)	100 W ultrasonicator,200 W Xenon lamp	90 Min	78 %	[59]
$BaTiO_3$-Ag_2O	RhB (5 mg/L)	750 W ultrasonicator, 220 W Halogen lamp	120 Min	~70 %	[60]
$BaTiO_3/WS_2$	OFL	300 W 40 kHz (ultrasonicator + LED light source)	100 Min	90 %	[61]
$BaTiO_3/Cd_{0.5}Zn_{0.5}S$	CIP (5 mg/l)	70 W Solar Simulator, 20 kHz ultrasonic	120 min	85 %	This Work

piezo-photocatalytic process demonstrates that 1.0BTO/CZS heterojunction synergistically combines the benefits of both photocatalytic and piezocatalytic processes, resulting in an efficient and catalytically active process for the oxidation of organic compounds. By comparing the correlation coefficient of the pseudo-first order and pseudo-second order model (Fig. 9(g-i)), it is evident that the system fits the pseudo-first-order model based on a higher correlation coefficient of 0.90632 (Table S4).

The efficiency of ciprofloxacin (CIP) degradation by the 1.0BTO/CZS heterostructure was significantly influenced by the solution's pH, as

shown in Fig. 10(a). The optimal pH for degradation was found to be 6. This behavior can be explained by considering two key factors. First, CIP is a weak base, and at higher pH, it becomes deprotonated, increasing the concentration of the target molecule available for degradation. However, excessively high pH (basic conditions) leads to CIP precipitation due to an abundance of hydroxide ions, reducing the available target molecule. Second, at very low pH, CIP becomes heavily protonated, and it is converted into its cationic state. This tends to hinder the catalyst performance due to the lack of mobility of the CIP within the solution, as indicated by the degradation analysis conducted at pH 2, which greatly reduced efficiency (Fig. 10(a)). Therefore, the observed decrease in efficiency at both high and low pH suggests a sweet spot around neutral pH (pH 6–7) for optimal CIP oxidation. This range balances the availability of CIP molecules and maintains favorable conditions for catalyst activity. Consequently, a pH of 6 was chosen for subsequent experiments to ensure the best performance of the 1.0BTO/CZS system. The reusability of the 1.0BTO/CZS catalyst was further explored for ciprofloxacin degradation (Fig. 10(b)), whereby the catalyst was centrifuged, dried, and used for the following cycle until all 4 cycles were completed. The catalyst maintained excellent performance after four cycles, achieving an average degradation efficiency of around 80 %. This slight decrease in efficiency may be due to some catalyst loss during recovery. Overall, the results demonstrate the effectiveness of 1.0BTO/CZS for CIP removal. Catalyst stability was further evaluated by repeating powder X-ray diffraction analysis of the fresh catalyst and the catalyst after the degradation reaction (Fig. 10(c)). The crystal structure of the catalyst was slightly changed, as indicated by the suppression of peaks and new splitting of integrated peaks. This can be the result of excessive use, surface etching, defect generation, mechanical stress-induced strain due to irradiation of ultrasonication, and leftover pollutants on the surface of the nanostructure. Much of the crystal structure remained intact, exhibiting the potential for further application and efficiency.

3.5. The mechanism for the enhanced piezo-photocatalytic performance

To understand the mechanism behind piezo-induced photocatalysis for CIP removal, radical trapping experiments were conducted. Scavengers were used to target specific reactive species: ethylenediaminetetraacetic acid disodium salt (EDTA) for holes (h^+), acrylamide for superoxides ($^{\bullet}O_2^-$), and tert-butanol (t-BuOH) for hydroxyl radicals ($^{\bullet}OH$). Fig. 11(a–b) shows a significant decrease in oxidation efficiency when h^+ was quenched with EDTA (over 50 % reduction). The EDTA interacts with the surface charge of the composite by complexing surface sites. Similarly, t-BuOH (hydroxyl radical scavenger) reduced efficiency by around 42 %, while acrylamide (superoxide scavenger) also inhibited degradation, bringing it down to 45.1 %. This means that superoxides and hydroxyls do contribute but are not the primary active oxidants. These results, with all scavengers causing performance reduction, suggest that all three oxidants contribute to CIP degradation. Notably, the quenching effect of h^+ was the strongest, indicating its major role. It's important to consider that some scavengers, particularly hydroxyl radical inhibitors, might degrade themselves under ultrasonic agitation [26]. To further elucidate the contribution of electrons in the mechanism and degradation pathway of CIP, all the scavengers were added to the solution under the same experimental conditions. Interestingly, 0 % of the pollutant was adsorbed and degraded after 90 min of contact time, irradiation, and illumination, highlighting the lack of contribution of the electrons except for the reduction of dissolved oxygen forming superoxides. Pertaining to the adsorption, The absence of adsorption suggests that the scavengers neutralized surface-active sites, blocking pollutant interaction with the catalyst. In the presence of $AgNO_3$, degradation was reduced to 76 %, indicating that electrons (e^-) play the least significant role in the degradation process. In addition, electrons (e^-) could have impacted the formation of superoxides, hence the high efficiency but still lower than the bare degradation. Second-highest adsorption, possibly because Ag^+ interacts with the catalyst surface, modifying charge distribution and enhancing pollutant binding. Both these analyses exhibit that the electrons have minimal effect on degradation due to the absence of removal in the presence of $AgNO_3$ and all scavengers.

Based on the previous discussions and characterizations, the degradation mechanism is illustrated in Fig. 12. The band gap energy was determined using the UV-DRS, and it was determined to be 2.20 eV and 2.87 eV for CZS and BTO, respectively. The Mott-Schottky was used to extrapolate the Fermi energy level of the as-prepared nanomaterials, and they were determined to be 0.18 and −0.429 V vs NHE. Applying the above-calculated values, the conduction bands (CB) for the pristine nanostructures were determined to be −0.73 V and −0.12 V vs. NHE, and the valence bands (VB) were 1.47 V and 2.75 V vs. NHE for CZS and BTO, respectively. It is noticeable that the Fermi energy level of CZS (reducing catalyst, RC) is significantly higher than that of BTO (oxidizing catalyst, OC), and due to that, electrons will flow from CZS to BTO, generating an electric field at the hetero-interface. Band positions derived from the XPS also indicated that the conduction band of CZS was placed lower than that of BTO, while the valence band of BTO is placed higher than that of CZS. Both the estimated band edge arrangements favour the S-Scheme charge transfer mechanism. Under illumination and ultrasound, the generated electrons from the CB of BTO migrate towards the VB of CZS, leaving the electrons in the CB of CZS active and holes in the VB of BTO active for redox reactions. The band bending of the components allows for efficient charge transfer between CZS and BTO. This heterostructure arrangement allows a substantial reduction potential of CZS and oxidation potential of BTO, resulting in enhanced piezo-photocatalytic performance. The generation of oxidants is summarized by Eqs. 12–17, whereby the electrons at CZS's CB reduce

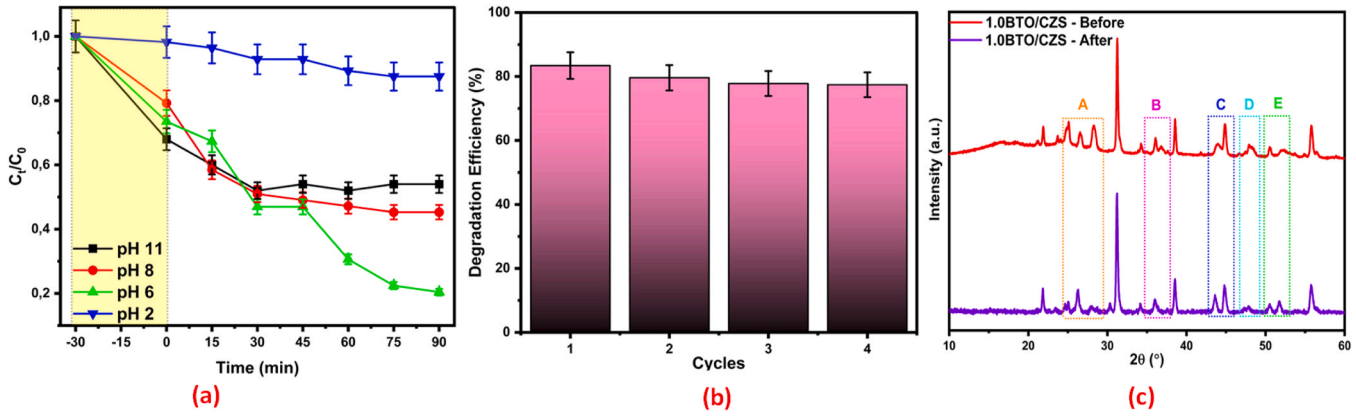

Fig. 10. (a) pH studies, (b) stability studies, and (c) wastewater analysis XRD.

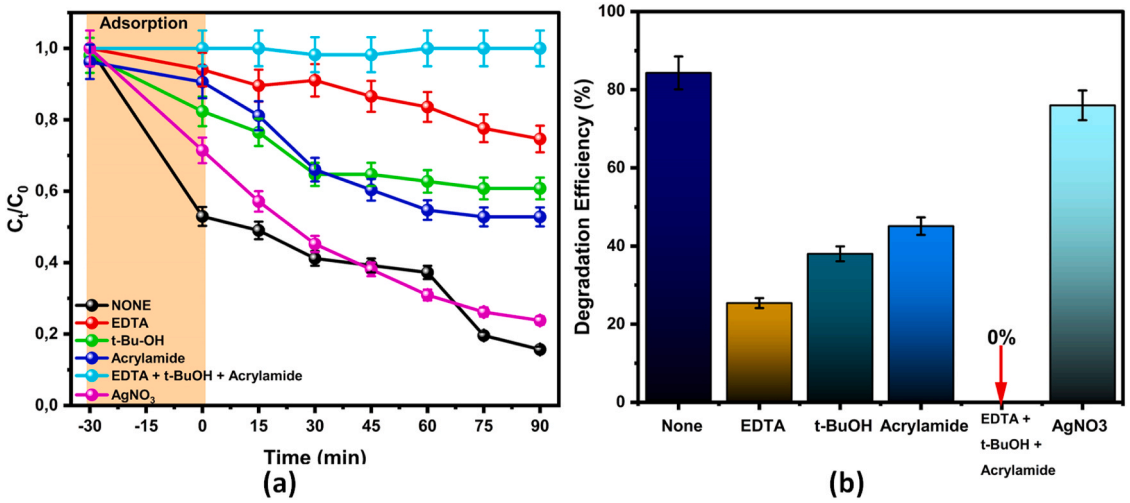

Fig. 11. (a-b) Piezo-photocatalytic oxidation contaminant degradation with 1.0BTO/CZS in the presence of EDTA-2Na, t-BuOH, acrylamide, and $AgNO_3$ scavengers.

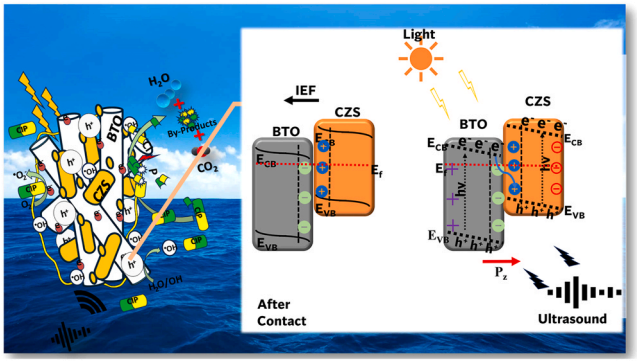

Fig. 12. Schematic illustration of the proposed mechanism of 1.0BTO/CZS S-Scheme heterojunction formation, charge carrier separation, and transfer.

oxygen to superoxides, while the holes in the VB of BTO oxidize water and hydroxyl ions into hydroxyl radicals. Holes in the VB of BTO also contribute to the mineralization of the pollutants, as indicated by our scavenger studies whereby EDTA was e, played to trap the holes, and the efficiency was greatly reduced. Cavitation provided by ultrasonication (US) triggers a process that breaks down water molecules in the solution into hydroxyl radicals. In this study, however, the •OH generated by the ultrasonic effect is insignificant, as indicated by the process of piezolysis, which resulted in an oxidation efficiency of 2 % after 90 min. This suggests that the hydroxyl radicals in the study are mostly generated by the oxidating catalyst (BTO) by cleaving water and oxidizing hydroxyl ions.

$$1.0BTO/CZS + hv + US \rightarrow e^- + h^+ \quad (12)$$

$$CZS(e^-) + O_2 \rightarrow {}^{\bullet}O_2^- \quad (13)$$

$$BTO(h^+) + OH^- \rightarrow {}^{\bullet}OH \quad (14)$$

$$US + H_2O \rightarrow {}^{\bullet}OH + H^+ \quad (15)$$

$$BTO(h^+) + H_2O \rightarrow {}^{\bullet}OH + H^+ \quad (16)$$

$${}^{\bullet}O_2^- + h^+ + {}^{\bullet}OH + CIP \rightarrow H_2O + CO_2 + \text{Small molecules} \quad (17)$$

3.6. Mineralization of ciprofloxacin in synthetic and real water samples using 1.0BTO/CZS

Total organic carbon (TOC) was employed in the determination of the mineralization of ciprofloxacin during the piezo-photocatalytic process after 90-minute intervals. The catalyst mass was maintained at 50 mg, ultrasound power at 20 W, and the light source (70 W) distance was kept at 10 mm from the solutions. The highest mineralization percentage was obtained for the synthetic water sample, reaching a maximum of 46.7 %, and the real water samples reached a maximum percentage of 38.8 % (Fig. 13). The reduction of the organic content in both the synthetic and real water samples indicates the synergistic relationship between the 1.0BTO/CZS catalyst and the piezo-photocatalysis degradation process in water. This data also implies that the hybrid process improves the charge separation within the S-Scheme heterostructure to allow efficient mineralization of CIP in water.

3.7. Proposed degradation pathway for ciprofloxacin

The degradation pathway of ciprofloxacin using 1.0BTO/CZS catalyst was studied using the fragments obtained from the chromatograms of UPLC-MS analysis. The chromatograms were obtained from the

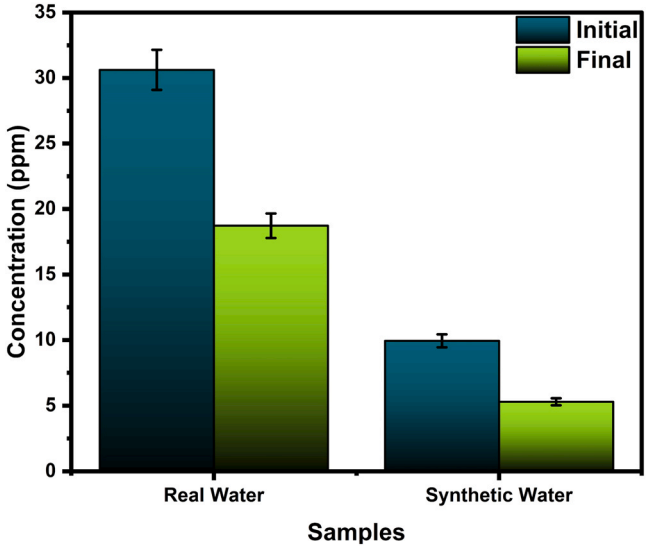

Fig. 13. TOC plots for synthetic and real water samples using 1.0BTO/CZS.

analysis of standard CIP solution aliquots collected every 30 min for 90 min. The standard CIP solution showed a prominent peak at 3.32 min ($m/z = 332$). Formed intermediates as a result of degradation of CIP for 90 min are shown in Fig. S10 indicated by m/z fragments on the chromatograms. Most prominent intermediates' products that were identified by the mass spectra include $m/z = 190$, $m/z = 202$, $m/z = 245$, $m/z = 362$, $m/z = 302$, $m/z = 202$, and $m/z = 274$. Identical degradation fragments have been reported [62–68]. Based on the fragments recorded from the UPLC-MS, 4 possible degradation mechanisms were identified based on the interaction of hydroxylation and other group activity of the molecule (Fig. 14). Pathway I highlights the generation of product 1 through defluorination, hydroxylation, and conversion to generate $m/z = 202$ (Fragment 1) moiety shown by Zhuoyao et al. [62]. Pathway II shows the generation of moiety $m/z = 362$ (Fragment 2), which can be a result of two processes: hydroxylation and dehydrogenation. Firstly, hydroxylation of the piperazine ring is followed by dehydrogenation to generate a carbonyl carbon; then, it is further hydroxylated to generate $m/z = 362$ [67], which further generates monoaldehyde moiety of $m/z = 302$ (Fragment 3) through a possible decarbonylation process where it lost both C-O groups. Fragment 4 ($m/z = 245$) was generated through the partial degradation of the piperazine moiety and defluorination process, similar to that reported by Taicheng et al. [69]. Complete degradation of the piperazine ring and cleavage of the cyclopropyl group results in the $m/z = 190$ moiety (Fragment 5). Pathway III proposes that the piperazine moiety is degraded and decarboxylation of the quinolone group are the typical pathways that lead to the formation of moiety $m/z = 274$ (Fragment 6). The fragment $m/z = 274$ went through further defluorination and carbon cleavage to form a similar moiety of $m/z = 245$ [69], which generates fragment 9 ($m/z = 202$) after the complete degradation of the piperazine moiety. The last pathway (IV) generates a similar moiety of $m/z = 274$ (Fragment 10), whereby this fragment is formed through decarboxylation.

3.8. Toxicology assessment and CIP fragments

The toxicology data of CIP and the degradation fragments were investigated using the Toxicity Estimation Software (T.E.S.T.). The T.E.S.T. software is an open-source toxicity tool developed by the Environmental Protection Agency in the U.S., which uses the properties of the compound materials based on the Quantitative Structure-Activity Relationships (QSARs) methods. Only the consensus method was used as it provides the average of all the other methods within the capabilities of the software. As shown in Table S5, developmental toxicity, mutagenicity, and oral rat LD_{50} were evaluated and compared to the parent CIP molecule. As expected, most of the intermediates had mutagenicity negative reports (0 <0.5), with the exception of intermediates of two moieties of $m/z = 274$ and $m/z = 245$, measuring above 0.5. Based on the developmental toxicity test, which is used for the investigation of molecule developmental influence in organisms, a molecule is regarded as developmentally toxic if the predicted value is above 0.5. There was a significant decrease in the toxicity of the intermediates compared to the parent CIP molecule. However, these intermediates are still considered toxic based on the determined values. This is further shown by the oral rat LD_{50} as most of the intermediates had a lower mg/kg predicted value, showing their toxicity towards rats.

4. Conclusion

In this work, we have fabricated an S-scheme heterostructure of $BaTiO_3/Cd_{0.5}Zn_{0.5}S$ nanorods via a facile solvothermal synthesis method. The CZS exhibited both photocatalytic and piezoelectric properties due to its 1-D structure, while BTO showed relatively good

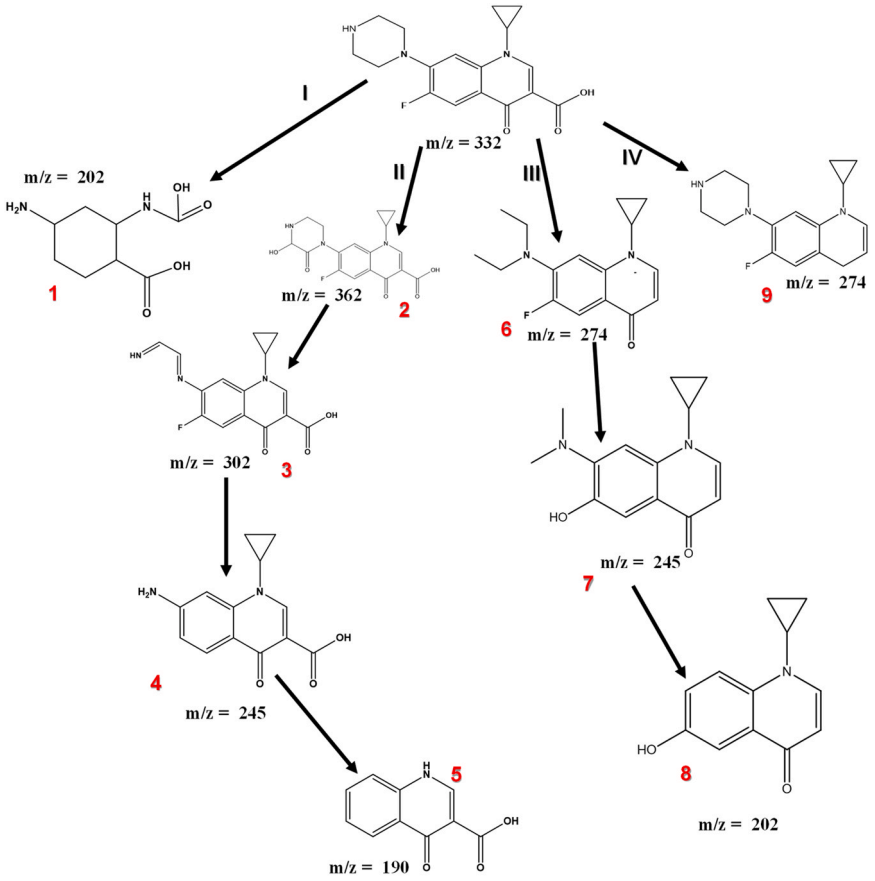

Fig. 14. Possible degradation pathways of CIP via piezo-photocatalysis.

piezoelectric properties because of its non-centrosymmetric nature. The synergy between these two nanostructures was observed through the piezo-photocurrent transient light response studies, indicating enhanced visible-light-induced charge carriers. The S-scheme arrangement, together with the piezo-photocatalytic process, allowed the conservation of enough holes and electrons for the generation of oxidants for the CIP degradation using 1.0BTO/CZS, hence its impressive degradation and stability in comparison to its induvial counterparts. This work offers new insights into the development of hybrid heterostructures for piezo-photocatalysis of organic waste in wastewater.

CRediT authorship contribution statement

Mabuba Nonhlangabezo: Writing – review & editing, Writing – original draft, Resources, Project administration, Conceptualization. **Mohlala Tshepo T.:** Writing – review & editing, Writing – original draft, Formal analysis, Data curation, Conceptualization. **Tunde L. Yusuf:** Writing – review & editing, Writing – original draft, Supervision, Conceptualization. **Masukume Mike:** Writing – original draft, Project administration. **Ojijo Vincent:** Writing – original draft, Project administration.

Declaration of Competing Interest

The authors declare that they have no known competing financial interests or personal relationships that could have appeared to influence the work reported in this paper.

Acknowledgments

We thank the Centre for Nanomaterials Science Research, University of Johannesburg (UJ), South Africa and the Faculty of Science. TTM is grateful to the Council of Research and Industrial Research (CSIR), South Africa, for the study grant CPRR Grant Number.

Appendix A. Supporting information

Supplementary data associated with this article can be found in the online version at doi:10.1016/j.jece.2025.116857.

Data availability

Data will be made available on request.

References

[1] B. Palanivel, C. Ayappan, V. Jayaraman, S. Chidambaram, R. Maheswaran, A. Mani, Inverse spinel NiFe2O4 deposited g-C3N4 nanosheet for enhanced visible light photocatalytic activity, Mater. Sci. Semicond. Process 100 (2019) 87–97, https://doi.org/10.1016/J.MSSP.2019.04.040.

[2] B.L. Phoon, C.C. Ong, M.S. Mohamed Saheed, P.L. Show, J.S. Chang, T.C. Ling, et al., Conventional and emerging technologies for removal of antibiotics from wastewater, J. Hazard. Mater. 400 (2020) 122961, https://doi.org/10.1016/J.JHAZMAT.2020.122961.

[3] M.P.C. Mora-Gamboa, S.M. Rincón-Gamboa, L.D. Ardila-Leal, R.A. Poutou-Piñales, A.M. Pedroza-Rodríguez, B.E. Quevedo-Hidalgo, Impact of antibiotics as waste, physical, chemical, and enzymatical degradation: use of laccases, Molecules (2022) 27, https://doi.org/10.3390/MOLECULES27144436.

[4] K.J. Choi, S.G. Kim, S.H. Kim, Removal of antibiotics by coagulation and granular activated carbon filtration, J. Hazard Mater. 151 (2008) 38–43, https://doi.org/10.1016/J.JHAZMAT.2007.05.059.

[5] V. Kumar, S.K. Dwivedi, A review on accessible techniques for removal of hexavalent Chromium and divalent Nickel from industrial wastewater: recent research and future outlook, J. Clean. Prod. 295 (2021) 126229, https://doi.org/10.1016/J.JCLEPRO.2021.126229.

[6] A. Babu Ponnusami, S. Sinha, H. Ashokan, M. V Paul, S.P. Hariharan, J. Arun, et al., Advanced oxidation process (AOP) combined biological process for wastewater treatment: a review on advancements, feasibility and practicability of combined techniques, Environ. Res. 237 (2023) 116944, https://doi.org/10.1016/J.ENVRES.2023.116944.

[7] V. Vinayagam, K.N. Palani, S. Ganesh, S. Rajesh, V.V. Akula, R. Avoodaiappan, et al., Recent developments on advanced oxidation processes for degradation of pollutants from wastewater with focus on antibiotics and organic dyes, Environ. Res. 240 (2024) 117500, https://doi.org/10.1016/J.ENVRES.2023.117500.

[8] S. Jia, Y. Su, B. Zhang, Z. Zhao, S. Li, Y. Zhang, et al., Few-layer MoS2 nanosheet-coated KNbO3 nanowire heterostructures: piezo-photocatalytic effect enhanced hydrogen production and organic pollutant degradation, Nanoscale 11 (2019) 7690–7700, https://doi.org/10.1039/C9NR00246D.

[9] W. Qi, Y. Fu, E. Liu, Z. Cheng, Y. Sun, S. Liu, et al., Advancements and opportunities in piezo-(photo)catalytic synthesis of value-added chemicals, EES Catal. 2 (2024) 884–910, https://doi.org/10.1039/D3EY00313B.

[10] H. Yu, Y. Ji, Y. Zhang, S. Tu, S.K. Boong, H.K. Lee, et al., Coupling enhanced piezo-photocatalysis on robust intergrowth ferroelectric SrBi8Ti7O27 nanosheets, ACS Sustain. Chem. Eng. (2024), https://doi.org/10.1021/ACSSUSCHEMENG.4C02771/SUPPL_FILE/SC4C02771_SI_001.PDF.

[11] N. Domingo, Understanding piezocatalysis, pyrocatalysis and ferrocatalysis, Front. Nanotechnol. 6 (2024) 1320503, https://doi.org/10.3389/FNANO.2024.1320503/BIBTEX.

[12] A. Pattnaik, J.N. Sahu, A.K. Poonia, P. Ghosh, Current perspective of nano-engineered metal oxide based photocatalysts in advanced oxidation processes for degradation of organic pollutants in wastewater, Chem. Eng. Res Des. 190 (2023) 667–686, https://doi.org/10.1016/J.CHERD.2023.01.014.

[13] F. Liang, Z. Chen, S. Sun, X. Ji, X. Wang, Synergistic piezo-photocatalysis on carbon nitride nanotubes for organic pollution elimination, J. Environ. Chem. Eng. 12 (2024) 112716, https://doi.org/10.1016/J.JECE.2024.112716.

[14] D. Masekela, T.L. Yusuf, S.A. Balogun, E. Makhado, O.I. Adeniran, K.D. Modibane, Interfacial engineering of MoS2 and bimetallic MOF hybrid for superior piezo-photocatalytic hydrogen production and wastewater treatment, J. Alloy. Compd. 1020 (2025) 179304, https://doi.org/10.1016/J.JALLCOM.2025.179304.

[15] K.F. Alshammari, Recent advances of piezo-catalysis and photocatalysis for efficient environmental remediation, Luminescence 39 (2024) e4808, https://doi.org/10.1002/BIO.4808.

[16] D. Masekela, N.C. Hintsho-Mbita, S. Sam, T.L. Yusuf, N. Mabuba, Application of BaTiO3-based catalysts for piezocatalytic, photocatalytic and piezo-photocatalytic degradation of organic pollutants and bacterial disinfection in wastewater: a comprehensive review, Arab J. Chem. 16 (2023) 104473, https://doi.org/10.1016/J.ARABJC.2022.104473.

[17] L. Jing, Y. Xu, M. Xie, Z. Li, C. Wu, H. Zhao, et al., Piezo-photocatalysts in the field of energy and environment: designs, applications, and prospects, Nano Energy 112 (2023) 108508, https://doi.org/10.1016/J.NANOEN.2023.108508.

[18] Q. Xu, L. Zhang, B. Cheng, J. Fan, J. Yu, S-scheme heterojunction photocatalyst, Chem 6 (2020) 1543–1559, https://doi.org/10.1016/J.CHEMPR.2020.06.010.

[19] S. Sambyal, R. Sharma, P. Mandyal, S. Balou, P. Gholami, B. Fang, et al., Advancement in two-dimensional carbonaceous nanomaterials for photocatalytic water detoxification and energy conversion, J. Environ. Chem. Eng. 11 (2023) 109517, https://doi.org/10.1016/J.JECE.2023.109517.

[20] X. Liu, Y. Li, H. Wang, J. Liu, J. Fu, J. Liu, et al., In situ construction of N-rich carbon nitride (C3N5)/silver phosphate (Ag3PO4) S-scheme heterojunctions for the efficient photocatalytic removal of levofloxacin antibiotic and RhB, Carbon Lett. (2024), https://doi.org/10.1007/s42823-024-00741-1.

[21] B. Wang, H. Yuan, T. Yang, P. Wang, X. Xu, J. Chang, et al., A two-dimensional PtS2/BN heterostructure as an S-scheme photocatalyst with enhanced activity for overall water splitting, Phys. Chem. Chem. Phys. 24 (2022) 26908–26914, https://doi.org/10.1039/D2CP03595B.

[22] P. Wang, S. Zhong, M. Lin, C. Lin, T. Lin, M. Gao, et al., Signally enhanced piezo-photocatalysis of Bi0.5Na0.5TiO3/MWCNTs composite for degradation of rhodamine B, Chemosphere 308 (2022) 136596, https://doi.org/10.1016/J.CHEMOSPHERE.2022.136596.

[23] L. Wang, J. Sun, B. Cheng, R. He, J. Yu, S-scheme heterojunction photocatalysts for H2O2 production, J. Phys. Chem. Lett. 14 (2023) 4803–4814, https://doi.org/10.1021/ACS.JPCLETT.3C00811/ASSET/IMAGES/MEDIUM/JZ3C00811_0014.GIF.

[24] R.T. Guo, S.H. Guo, L.Q. Yu, W.G. Pan, Recent progress and perspectives of S-scheme heterojunction photocatalysts for photocatalytic CO2 reduction, Energy Fuels 38 (2024) 869–894, https://doi.org/10.1021/ACS.ENERGYFUELS.3C04118/ASSET/IMAGES/MEDIUM/EF3C04118_0026.GIF.

[25] O.C. Olatunde, I. Waziri, D.C. Onwudiwe, T.L. Yusuf, Design of S-scheme CuInS2/CeO2 heterojunction for enhanced photocatalytic degradation of pharmaceuticals in wastewater, Langmuir (2025), https://doi.org/10.1021/ACS.LANGMUIR.4C04175/ASSET/IMAGES/LARGE/LA4C04175_0008.JPEG.

[26] X. Zhou, S. Wu, C. Li, F. Yan, H. Bai, B. Shen, et al., Piezophototronic effect in enhancing charge carrier separation and transfer in ZnO/BaTiO3 heterostructures for high-efficiency catalytic oxidation, Nano Energy 66 (2019) 104127, https://doi.org/10.1016/J.NANOEN.2019.104127.

[27] E. Mancuso, L. Shah, S. Jindal, C. Serenelli, Z.M. Tsikriteas, H. Khanbareh, et al., Additively manufactured BaTiO3 composite scaffolds: a novel strategy for load bearing bone tissue engineering applications, Mater. Sci. Eng. C 126 (2021) 112192, https://doi.org/10.1016/J.MSEC.2021.112192.

[28] Li L., Salvador P.A., Rohrer G.S. Photocatalysts with Internal Electric Fields 2014. https://doi.org/10.1039/c3nr03998f.

[29] J. Wu, N. Qin, D. Bao, Effective enhancement of piezocatalytic activity of BaTiO3 nanowires under ultrasonic vibration, Nano Energy 45 (2018) 44–51, https://doi.org/10.1016/J.NANOEN.2017.12.034.

[30] B. Fu, J. Li, H. Jiang, X. He, Y. Ma, J. Wang, et al., Modulation of electric dipoles inside electrospun BaTiO3@TiO2 core-shell nanofibers for enhanced piezo-photocatalytic degradation of organic pollutants, Nano Energy 93 (2022) 106841, https://doi.org/10.1016/J.NANOEN.2021.106841.

[31] S. Lan, X. Zeng, R.A. Rather, I.M.C. Lo, Enhanced trimethoxypyrimidine degradation by piezophotocatalysis of BaTiO3/Ag3PO4 using mechanical vibration and visible light simultaneously, Environ. Sci. Nano 6 (2019) 554–564, https://doi.org/10.1039/C8EN01192C.
[32] Z. Chen, G. Li, X. Zheng, Y. Liu, J. Dai, B. Huang, et al., Facile synthesis of advanced BaTiO3/CuPbSbS3 heterostructure photocatalyst with enhanced piezo-photocatalytic degradation performance, Nano Energy 124 (2024) 109463, https://doi.org/10.1016/J.NANOEN.2024.109463.
[33] H. Zheng, X. Li, K. Zhu, P. Liang, M. Wu, Y. Rao, et al., Semiconducting BaTiO3@C core-shell structure for improving piezo-photocatalytic performance, Nano Energy 93 (2022) 106831, https://doi.org/10.1016/J.NANOEN.2021.106831.
[34] Q. Zhu, J. Wang, S. Chen, H. Fu, J. Zhang, H. Gao, et al., Effect of the organic sulfur source on the photocatalytic activity of CdS, RSC Adv. 12 (2022) 11262–11271, https://doi.org/10.1039/D2RA01309F.
[35] T.L. Yusuf, O.C. Olatunde, D. Masekela, N. Mabuba, D.C. Onwudiwe, S. Makgato, Rational design of S-scheme Cd0.5Zn0.5S/CeO2 heterojunction for enhanced photooxidation of antibiotics and photoreduction of Cr(VI), Ceram. Int 50 (2024) 45581–45591, https://doi.org/10.1016/J.CERAMINT.2024.08.397.
[36] S. Sun, D. Ren, M. Yang, J. Cui, Q. Yang, S. Liang, In-situ construction of direct Z-scheme sea-urchin-like ZnS/SnO2 heterojunctions for boosted photocatalytic hydrogen production, Int J. Hydrog. Energy 47 (2022) 9201–9208, https://doi.org/10.1016/J.IJHYDENE.2021.12.249.
[37] J. Kundu, D.D. Mal, D. Pradhan, Single-step solvothermal synthesis of highly uniform CdxZn1−xS nanospheres for improved visible light photocatalytic hydrogen generation, Inorg. Chem. Front. 8 (2021) 3055–3065, https://doi.org/10.1039/D0QI00531B.
[38] M.B. Muradov, L.R. Gahramanli, O.O. Balayeva, I.N. Nasibov, G.M. Eyvazova, I. R. Amiraslanov, et al., Formation mechanism of CdxZn1-xS/PVA nanocomposites by SILAR method, Results Phys. 18 (2020) 103280, https://doi.org/10.1016/J.RINP.2020.103280.
[39] D. Chawla, N. Goswami, Structural and optical properties of CdZnS nanoparticles by exploding wire technique, Mater. Today Proc. 28 (2020) 278–281, https://doi.org/10.1016/J.MATPR.2020.02.071.
[40] K. He, ZnO/ZnS/CdS three-phase composite photocatalyst with a flower cluster structure: research on its preparation and photocatalytic activity hydrogen production, Int. J. Hydrog. Energy 51 (2024) 30–40, https://doi.org/10.1016/J.IJHYDENE.2023.08.050.
[41] M. Masab, H. Muhammad, F. Shah, M. Yasir, M. Hanif, Facile synthesis of CdZnS QDs: effects of different capping agents on the photoluminescence properties, Mater. Sci. Semicond. Process 81 (2018) 113–117, https://doi.org/10.1016/J.MSSP.2018.03.023.
[42] X. Liu, Y. Jiang, L. Zhang, Y. Zhang, Y. Li, X. Xu, et al., In-situ construction of Mo3S4/Cd0.5Zn0.5S heterojunction: an efficient and stable photocatalyst for H2 evolution, Int. J. Hydrog. Energy 45 (2020) 21014–21023, https://doi.org/10.1016/J.IJHYDENE.2020.05.249.
[43] D. Masekela, S.A. Balogun, T.L. Yusuf, S. Makgato, K.D. Modibane, Advancements in piezo-photocatalysts for sustainable hydrogen generation and pollutant degradation: a comprehensive overview of piezo-photocatalysis, J. Water Process Eng. 71 (2025) 107172, https://doi.org/10.1016/J.JWPE.2025.107172.
[44] H. Gong, Z. Li, Z. Chen, Q. Liu, M. Song, C. Huang, NiSe/Cd0.5Zn0.5S composite nanoparticles for use in p-n heterojunction-based photocatalysts for solar energy harvesting, ACS Appl. Nano Mater. 3 (2020) 3665–3674, https://doi.org/10.1021/ACSANM.0C00388/SUPPL_FILE/AN0C00388_SI_001.PDF.
[45] I.C. Amaechi, G. Kolhatkar, A.H. Youssef, D. Rawach, S. Sun, A. Ruediger, B-site modified photoferroic Cr3+-doped barium titanate nanoparticles: microwave-assisted hydrothermal synthesis, photocatalytic and electrochemical properties, RSC Adv. 9 (2019) 20806–20817, https://doi.org/10.1039/C9RA03439K.
[46] M.F. Mehmood, A. Habib, Hydrothermal synthesis and structural characterization of BaTiO3 powder, Nucleus 60 (2023) 168–173.
[47] Vijayalakshmi R., Rajendran V. Synthesis of BaTiO 3 and Evaluation of Optical Properties 2010:1–11.
[48] H. Alnoor, A. Savoyant, X. Liu, G. Pozina, M. Willander, O. Nur, An effective low-temperature solution synthesis of Co-doped [0001]-oriented ZnO nanorods, J. Appl. Phys. (2017) 121, https://doi.org/10.1063/1.4984314/144868.
[49] J. Liu, S. Zhang, D. Qu, X. Zhou, M. Yin, C. Wang, et al., Defects-rich heterostructures trigger strong polarization coupling in sulfides/carbon composites with robust electromagnetic wave absorption, Nano-Micro Lett. 17 (2025) 1–20, https://doi.org/10.1007/S40820-024-01515-0/FIGURES/6.
[50] M. Li, X. Tu, Y. Wang, Y. Su, J. Hu, B. Cai, et al., Highly enhanced visible-light-driven photoelectrochemical performance of ZnO-modified In2S3 nanosheet arrays by atomic layer deposition, Nano-Micro Lett. 10 (2018) 1–12, https://doi.org/10.1007/S40820-018-0199-Z/FIGURES/8.
[51] Y. Dong, S. Dong, B. Liu, C. Yu, J. Liu, D. Yang, et al., 2D piezoelectric Bi2MoO6 nanoribbons for GSH-enhanced sonodynamic therapy, Adv. Mater. 33 (2021) 2106838, https://doi.org/10.1002/ADMA.202106838.
[52] Cadmium Sulfide (CdS) Semiconductors n.d. ⟨https://www.azom.com/article.aspx?ArticleID= 8407⟩ (accessed 15 March 2025).
[53] D.N. Shevarenkov, A.F. Shchurov, Dielectric properties of polycrystalline ZnS, Semiconductors 40 (2006) 33–35, https://doi.org/10.1134/S1063782606010040/METRICS.
[54] A.O. Onjwaya, M.L. Malati, J.C. Ngila, L.N. Dlamini, Interfacial engineering of a multijunctional In2O3/WO3@Ti4N3Tx S-scheme photocatalyst with enhanced photoelectrochemical properties, Dalt Trans. 53 (2024) 7694–7710, https://doi.org/10.1039/D4DT00135D.
[55] S. Lin, S. Li, H. Huang, H. Yu, Y. Zhang, Synergetic piezo-photocatalytic hydrogen evolution on CdxZn1-xS solid-solution 1D nanorods, Small 18 (2022) 2106420, https://doi.org/10.1002/SMLL.202106420.
[56] Y. Li, R. Li, Y. Zhai, Y. Huang, S. Lee, J. Cao, Improved photocatalytic activity of BaTiO3/La2Ti2O7 heterojunction composites via piezoelectric-enhanced charge transfer, Appl. Surf. Sci. 570 (2021) 151146, https://doi.org/10.1016/J.APSUSC.2021.151146.
[57] D. Masekela, N.C. Hintsho-Mbita, N. Mabuba, Application of a piezo-photocatalytic thin film (FTO/BaTiO3/SnO2) for enhanced degradation of organic pollutants and disinfection of wastewater, Ceram. Int 49 (2023) 7566–7579, https://doi.org/10.1016/J.CERAMINT.2022.10.251.
[58] D. Masekela, N.C. Hintsho-Mbita, B. Ntsendwana, N. Mabuba, Thin films (FTO/BaTiO3/AgNPs) for enhanced piezo-photocatalytic degradation of methylene blue and Ciprofloxacin in wastewater, ACS Omega 7 (2022) 24329–24343, https://doi.org/10.1021/ACSOMEGA.2C01699/ASSET/IMAGES/LARGE/AO2C01699_0008.JPEG.
[59] C. Yu, M. Tan, C. Tao, Y. Hou, C. Liu, H. Meng, et al., Remarkably enhanced piezo-photocatalytic performance in BaTiO3/CuO heterostructures for organic pollutant degradation, J. Adv. Ceram. 11 (2022) 414–426, https://doi.org/10.1007/S40145-021-0544-4/METRICS.
[60] S. Thangavel, P. Pazhamalai, K. Krishnamoorthy, Y. Sivalingam, D. Arulappan, V. Mohan, et al., Ferroelectric-semiconductor BaTiO3–Ag2O nanohybrid as an efficient piezo-photocatalytic material, Chemosphere 292 (2022) 133398, https://doi.org/10.1016/J.CHEMOSPHERE.2021.133398.
[61] A. Fazli, F. Zakeri, A. Khataee, Y. Orooji, A BaTiO3/WS2 composite for piezo-photocatalytic persulfate activation and ofloxacin degradation, Commun. Chem. 5 (2022) 1–14, https://doi.org/10.1038/s42004-022-00707-2, 51 2022.
[62] Z. Chen, W. Lai, Y. Xu, G. Xie, W. Hou, P. Zhanchang, et al., Anodic oxidation of ciprofloxacin using different graphite felt anodes: kinetics and degradation pathways, J. Hazard Mater. 405 (2021) 124262, https://doi.org/10.1016/J.JHAZMAT.2020.124262.
[63] A.V. Karim, A. Shriwastav, Degradation of ciprofloxacin using photo, sono, and sonophotocatalytic oxidation with visible light and low-frequency ultrasound: Degradation kinetics and pathways, Chem. Eng. J. 392 (2020) 124853, https://doi.org/10.1016/J.CEJ.2020.124853.
[64] X. Hu, X. Hu, Q. Peng, L. Zhou, X. Tan, L. Jiang, et al., Mechanisms underlying the photocatalytic degradation pathway of ciprofloxacin with heterogeneous TiO2, Chem. Eng. J. 380 (2020) 122366, https://doi.org/10.1016/J.CEJ.2019.122366.
[65] X.J. Wen, C.G. Niu, L. Zhang, C. Liang, H. Guo, G.M. Zeng, Photocatalytic degradation of ciprofloxacin by a novel Z-scheme CeO2–Ag/AgBr photocatalyst: influencing factors, possible degradation pathways, and mechanism insight, J. Catal. 358 (2018) 141–154, https://doi.org/10.1016/J.JCAT.2017.11.029.
[66] H. se Ou, J. shao Ye, S. Ma, C. hai Wei, N. yun Gao, J. zhao He, Degradation of ciprofloxacin by UV and UV/H2O2 via multiple-wavelength ultraviolet light-emitting diodes: effectiveness, intermediates and antibacterial activity, Chem. Eng. J. 289 (2016) 391–401, https://doi.org/10.1016/J.CEJ.2016.01.006.
[67] X.X. Zhang, R. Li, M. Jia, S. Wang, Y. Huang, C. Chen, Degradation of ciprofloxacin in aqueous bismuth oxybromide (BiOBr) suspensions under visible light irradiation: a direct hole oxidation pathway, Chem. Eng. J. 274 (2015) 290–297, https://doi.org/10.1016/J.CEJ.2015.03.077.
[68] M. Chen, J. Yao, Y. Huang, H. Gong, W. Chu, Enhanced photocatalytic degradation of ciprofloxacin over Bi2O3/(BiO)2CO3 heterojunctions: efficiency, kinetics, pathways, mechanisms and toxicity evaluation, Chem. Eng. J. 334 (2018) 453–461, https://doi.org/10.1016/J.CEJ.2017.10.064.
[69] T. An, H. Yang, G. Li, W. Song, W.J. Cooper, X. Nie, Kinetics and mechanism of advanced oxidation processes (AOPs) in degradation of ciprofloxacin in water, Appl. Catal. B Environ. 94 (2010) 288–294, https://doi.org/10.1016/J.APCATB.2009.12.002.